HEART FAILURE

Central-acting therapeutics alleviate respiratory weakness caused by heart failure–induced ventilatory overdrive

Andrew J. Foster,[1]* Mathew J. Platt,[1]* Jason S. Huber,[1] Ashley L. Eadie,[2] Alicia M. Arkell,[1] Nadya Romanova,[1] David C. Wright,[1] Todd E. Gillis,[3] Coral L. Murrant,[1] Keith R. Brunt,[2†] Jeremy A. Simpson[1†]

Diaphragmatic weakness is a feature of heart failure (HF) associated with dyspnea and exertional fatigue. Most studies have focused on advanced stages of HF, leaving the cause unresolved. The long-standing theory is that pulmonary edema imposes a mechanical stress, resulting in diaphragmatic remodeling, but stable HF patients rarely exhibit pulmonary edema. We investigated how diaphragmatic weakness develops in two mouse models of pressure overload–induced HF. As in HF patients, both models had increased eupneic respiratory pressures and ventilatory drive. Despite the absence of pulmonary edema, diaphragmatic strength progressively declined during pressure overload; this decline correlated with a reduction in diaphragm cross-sectional area and preceded evidence of muscle weakness. We uncovered a functional codependence between angiotensin II and β-adrenergic (β-ADR) signaling, which increased ventilatory drive. Chronic overdrive was associated with increased PERK (double-stranded RNA–activated protein kinase R–like ER kinase) expression and phosphorylation of EIF2α (eukaryotic translation initiation factor 2α), which inhibits protein synthesis. Inhibition of β-ADR signaling after application of pressure overload normalized diaphragm strength, *Perk* expression, EIF2α phosphorylation, and diaphragmatic cross-sectional area. Only drugs that were able to penetrate the blood-brain barrier were effective in treating ventilatory overdrive and preventing diaphragmatic atrophy. These data provide insight into why similar drugs have different benefits on mortality and symptomatology, despite comparable cardiovascular effects.

INTRODUCTION

Heart failure (HF) is a major public health issue and a worldwide epidemic (*1*, *2*). Globally, HF has a prevalence of more than 23 million (*3*) and is increasing (*4*), with a lifetime risk of one in five (*3*) and a 5-year mortality of 50% (*3*). Respiratory complications of HF, such as dyspnea and exertional fatigue, are symptoms that impair quality of life and feature prominently in the clinical classification of HF. Dyspnea has been attributed to a variety of factors, including impaired lung mechanics (*5*–*10*), elevated ventilatory drive (*5*, *11*, *12*), and impaired diaphragmatic structure and function (*9*, *13*–*16*). The quality of life for HF patients remains poor, highlighting the need to understand the pathogenesis of HF-associated respiratory complications.

Diaphragmatic weakness is a salient feature of both HF patients (*13*–*16*) and disease models (*17*–*19*). A shift toward oxidative metabolism (*20*), atrophy (*21*, *22*), impaired calcium handling (*23*, *24*), and contractile dysfunction (*17*–*19*, *25*) are associated with diaphragmatic weakness. Yet, previous studies have focused on advanced stages of HF, leaving the incipient cause of diaphragmatic weakness undetermined.

The diaphragmatic features are similar between patients with HF and chronic obstructive pulmonary disease (COPD); therefore, a common mechanism has been proposed. COPD and HF both feature a chronic, unrelenting increase in the work of breathing, which is thought to drive the development of diaphragmatic weakness. In COPD, airway obstruction imposes a mechanical load on the diaphragm. The resistive stress on the respiratory muscles increases the energy cost of breathing, as estimated by the tension-time index (TTI). TTI is a product of the ratio of the mean diaphragmatic pressure (P) per breath (P_I) over the maximal pressure-generating capacity of the diaphragm (P_{Imax}) and the fraction of the breathing cycle time spent in inspiration (that is, the duty cycle; T_I/T_{total}) (*26*). In HF, the TTI is also chronically elevated (*14*).

Although it is easy to understand how increased airway resistance elevates TTI in COPD, airway resistance is not increased in HF. It is generally thought that the development of pulmonary edema in HF increases TTI. However, even in HF patients with severe hemodynamic congestion, pulmonary rales or edema are rare (*27*–*29*). Given that pulmonary edema is uncommon, it is unlikely the cause for elevated TTI in HF patients.

Here, we identify the incipient cause and molecular mechanisms of progressive diaphragm weakness in two mouse models of HF. We demonstrate that elevated TTI is caused by a central neurohormonal pathway that stimulates ventilatory overdrive (that is, a persistent increase in ventilatory drive triggering diaphragmatic myopathy). We also show that only select pharmacological agents are effective in treating ventilatory overdrive and subsequent development of diaphragmatic weakness. Our findings reconcile the reported benefits of certain angiotensin II (ANGII) receptor blockers (ARBs) and β-adrenergic (β-ADR) blockers within the same drug class (*30*, *31*). Diaphragmatic atrophy is preventable in HF, suggesting that early intervention could reduce dyspnea and improve the patient's overall quality of life.

RESULTS

Pressure overload–induced HF causes diaphragmatic weakness in mice

To verify the development of pressure overload–induced HF, we obtained invasive hemodynamic measures and histomorphometric

[1]Department of Human Health and Nutritional Science, University of Guelph, Guelph, Ontario N1G 2W1, Canada. [2]Department of Pharmacology, Dalhousie Medicine, Saint John, New Brunswick E2L 4L5, Canada. [3]Department of Integrative Biology, University of Guelph, Guelph, Ontario N1G 2W1, Canada.
*These authors contributed equally to this work.
†Corresponding author. Email: jeremys@uoguelph.ca (J.A.S.); keith.brunt@dal.ca (K.R.B.)

analysis of cardiac tissue and histomorphometric analysis of lung and diaphragm tissues after 18 weeks of pressure overload caused by experimental transverse aortic constriction (TAC) in male CD-1 mice (Fig. 1A and table S1). Pressure overload refers to a condition in which the heart muscle must contract to overcome an excessive afterload during systole. As expected, histological and morphometric analyses revealed ventricular hypertrophy and chamber dilatation (Fig. 1, B and C). Invasive hemodynamic measurements revealed systolic and diastolic dysfunction, as indicated by decreased contractility (dP/dt_{max}; Fig. 1D) and increased left ventricular end diastolic pressure (Fig. 1E), respectively.

To assess diaphragmatic weakness, we investigated the diaphragm's ability to generate P_{Imax}. The P_{Imax} (a volitional maneuver) cannot be measured in mice, so we measured the maximum inspiratory pressure generated during a 25-s tracheal occlusion (P_{Iocc}) as a surrogate of P_{Imax}. P_{Iocc} was reduced in our model, confirming the presence of diaphragmatic weakness (Fig. 1F). In patients with HF, TTI ($[P_I/P_{Imax}]*[T_I/T_{total}]$) at rest is increased as a result of lowered P_{Imax} (or P_{Iocc} in rodents) and elevated quiet resting pressure generation (P_I) with no change in duty cycle (T_I/T_{Total}) (*14*, *32*). We also confirmed an increased P_I during quiet breathing (Fig. 1G) with no change in duty cycle (Fig. 1H). Thus, our model recapitulates the diaphragmatic weakness and elevated TTI observed in HF patients.

We then evaluated the effect of HF on diaphragm structure and function. Histological analysis (Fig. 1I) revealed decreased muscle fiber CSA (Fig. 1J), along with increased fibrosis (Fig. 1K) in mice subjected to 18 weeks of TAC. However, in vitro diaphragm force production was preserved at 18 weeks of TAC (Fig. 1L). We accounted for any potential effect of atrophy on in vitro diaphragm function by normalizing force production to CSA. Hence, reduced muscle mass (with preserved force production), not decreased intrinsic myocyte force production, was the primary cause of diaphragmatic weakness.

Pulmonary edema has long been thought to be the cause of elevated TTI in HF patients. Whereas histological assessment showed changes in the lung morphology (fibrosis and leukocyte infiltrate) in advanced stages of TAC (9 weeks; Fig. 1M), there was no evidence of pulmonary

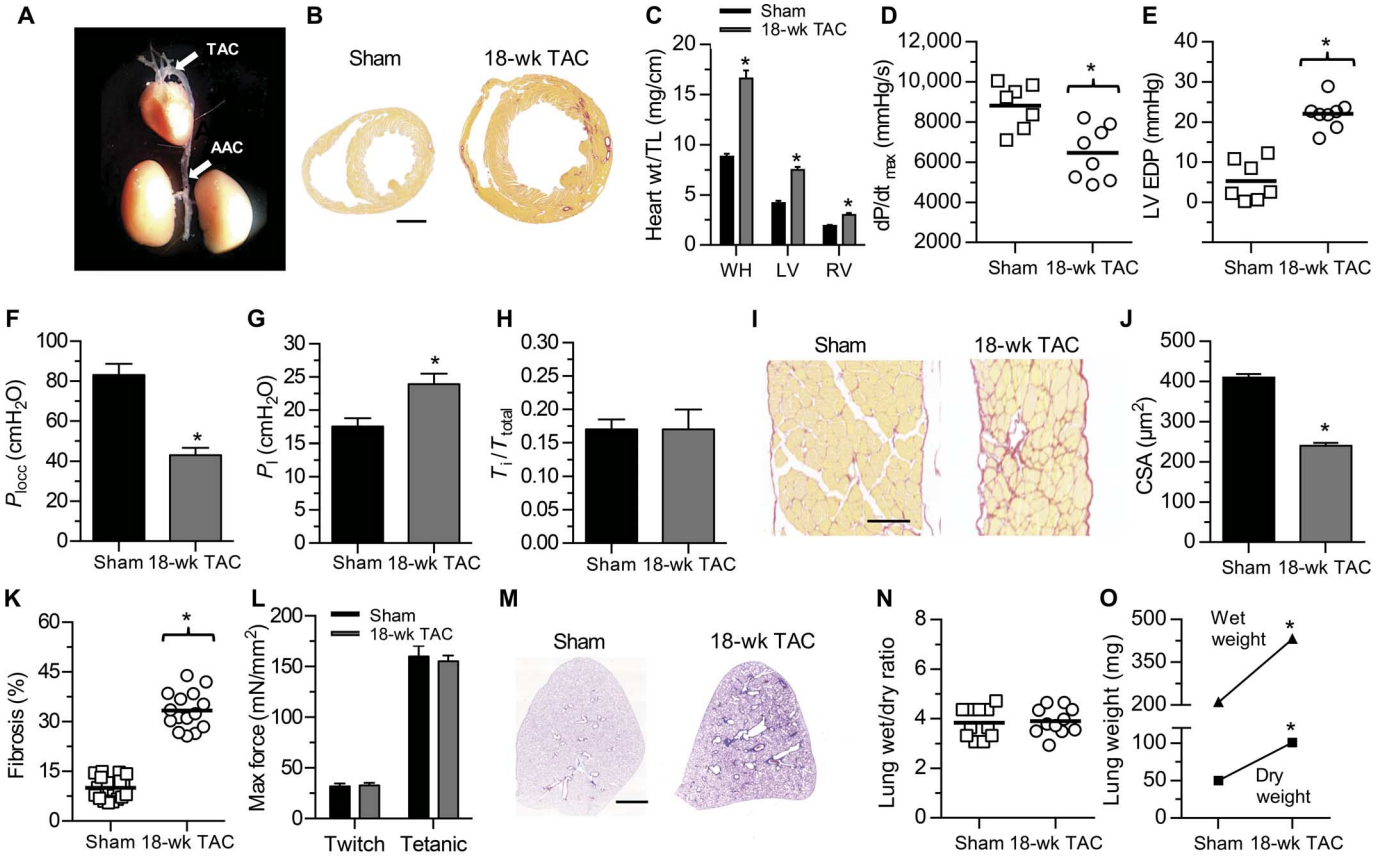

Fig. 1. End-stage pressure overload HF induces diaphragmatic myopathy, elevated ventilatory drive, and pulmonary remodeling in the absence of pulmonary edema. (**A**) Point of constriction on the transverse and abdominal aorta for experimental cardiac pressure overload. (**B**) Representative cross-sectional images of sham and 18-week TAC hearts at the mid-papillary region and stained with picrosirius red. (**C**) Normalized cardiac weights of whole heart (WH), left ventricle (LV), and right ventricle (RV) of sham (n = 8) and 18-week TAC (n = 8) mice. (**D** and **E**) The first derivative of pressure development (D) and left ventricular pressure (E) in sham (n = 8) and 18-week TAC (n = 8) mice. EDP, end-diastolic pressure. (**F**) In vivo maximal inspiratory pressure of sham (n = 10) and 18-week TAC (n = 6) mice during a 25-s airway occlusion. (**G**) In vitro force production of diaphragm from sham (n = 12) and 18-week TAC (n = 10) mice. (**H**) Duty cycle of sham (n = 8) and 18-week TAC (n = 5) mice. (**I**) Representative images of sham and 18-week TAC diaphragms stained with picrosirius red. (**J**) Cross-sectional area (CSA) of diaphragm muscle fibers in sham (n = 5) and 18-week TAC (n = 5) mice. (**K**) Percent fibrosis of sham (n = 5) and 18-week TAC (n = 5) diaphragms. (**L**) Twitch and tetanic diaphragmatic forces for sham (n = 5) and 18-week TAC (n = 5) mice. (**M**) Whole lungs of sham and 18-week TAC mice perfusion fixed at 20 cmH_2O and stained with Gomori's trichrome. (**N**) Wet weight–to–dry weight ratio of lungs from sham (n = 8) and 18-week TAC (n = 8) mice. (**O**) Wet and dry weights of sham (n = 8) and 18-week TAC (n = 8) lungs. Mean ± SEM; *Significance versus sham; $P < 0.05$, as determined by Student's t test. Scale bars, 2 mm (B), 100 μm (I), and 100 μm (M).

edema (lung wet/dry weight ratio) at any time point (Fig. 1, N and O). Together, these findings show that chronic pressure overload in mice recapitulates diaphragmatic weakness, atrophy, and increased resting pressure that is characteristic of patients with HF—yet with no evidence of pulmonary edema.

Diaphragmatic weakness occurs early and is caused by diaphragm atrophy

Diaphragmatic weakness (that is, reduced P_{Iocc}), atrophy (that is, reduced CSA), and fibrosis (Fig. 1, F and I to K) coexisted by 18 weeks of TAC. Therefore, we investigated the development of these defects during the pathogenesis of HF (Fig. 2). P_{Iocc} in mice at 2 weeks of TAC was similar to that of sham mice but fell by 4 weeks and further by 18 weeks (Fig. 2, A to C). Diaphragm CSA was significantly reduced at 4, 9, and 18 weeks of TAC (Fig. 2, D and E), and fibrosis was increased at all time points as compared to sham animals (fig. S1). To determine the effects of atrophy and fibrosis on intrinsic diaphragmatic function, we evaluated isolated muscle for in vitro force generation, rate of force production (dT/dt_{max}), relaxation (that is, passive baseline force), and resistance to fatigue. Unexpectedly, force production (fig. S2) was transiently enhanced at 2 weeks of TAC and showed no evidence of impairment at any time point that would contribute to diaphragmatic weakness.

The diaphragm is the primary inspiratory muscle, and therefore, pathological remodeling that affects its structure has direct effects on ventilation. The change in P_{Iocc} paralleled the progression of atrophy, and stepwise linear regression revealed that P_{Iocc} was linearly and strongly correlated with muscle CSA ($r^2 = 0.98$, $P < 0.05$; Fig. 2F). Reductions in P_{Iocc} were not attributable to necrosis or apoptosis because the number of muscle fibers spanning the diaphragm (abdominal to thoracic surfaces) was unchanged throughout the development of HF, and we did not find any centrally located nuclei or lesions. Thus, atrophy (Fig. 2, D and E) primarily accounted for the inability of the diaphragm to generate P_{Iocc} throughout the progression of HF (Fig. 2, B and C).

Chronic hypoperfusion of skeletal muscle can cause atrophy. The perfusing arteries of the diaphragm (pericardiophrenic, musculophrenic, and inferior/superior phrenic arteries) arise distal to the constriction in TAC. Thus, a transient decline in diaphragmatic perfusion pressure might result in hypoperfusion-induced atrophy. To rule out this possibility, we also used abdominal aortic constriction (AAC) to induce pressure overload (Fig. 1A). At 18 weeks of AAC, we observed a cardiac phenotype that was similar to 9 weeks of TAC (table S2). This finding is consistent with the distance of the constriction from the heart because AAC imposes a less severe hypertensive stress on the left ventricle (*33*). The diaphragms of mice after 18 weeks of AAC showed fibrosis and reduced CSA (fig. S3). Therefore, we concluded that the diaphragmatic atrophy and fibrosis observed in the TAC model did not result from hypotension-induced hypoperfusion.

A neurohormonal-induced increase in ventilatory drive causes diaphragmatic atrophy

To uncover the incipient cause of diaphragmatic atrophy, we investigated whether the stress-causing atrophy was a global phenomenon for all skeletal muscles or was specific to the diaphragm. We assessed the CSA of soleus (predominantly a slow-twitch muscle) and gastrocnemius (predominantly a fast-twitch muscle) lower-limb muscles from 4-week TAC mice (fig. S4), and it was unchanged in both limb muscles. Therefore, the incipient mechanism that drives atrophy was not systemic but rather a stress specifically affecting the diaphragm. Increased resting P_I is a diaphragm-specific stress. Although the long-standing theory has been that pulmonary edema increases P_I, we had already ruled this out in our model (Fig. 1N and table S1).

Lung remodeling and reductions in lung compliance (that is, increased lung stiffness) exist in advanced stages of HF (*7*) and could increase P_I. We observed a proportional increase in both the lung wet and dry weights of 18-week TAC mice (Fig. 1O), indicative of pulmonary remodeling. As such, we investigated the progressive changes in lung structure and mechanics to determine whether the physiological mechanism for diaphragm atrophy and increased P_I was due to a pulmonary remodeling–induced mechanical load. In the temporal analysis of lung weights, there was no evidence of transient pulmonary edema (Fig. 3A and table S1). Representative lung sections stained with Gomori's one-step trichrome are profiled in Fig. 3B. We identified a significant increase in pulmonary fibrosis after 9 and 18 weeks of TAC (Fig. 3C) along with a rightward shift in alveolar CSA (Fig. 3D), indicating pulmonary remodeling. To ascertain whether lung mechanics were altered by lung fibrosis, we generated lung compliance curves in mice by recording airway pressure in response to stepwise inflations with known volumes of air. Aligning with the histological data, dynamic lung compliance was significantly decreased after only 9 and 18 weeks of TAC (Fig. 3, E and F). The physiological cause of diaphragmatic atrophy must coincide with or precede the measured atrophy at 4 weeks of TAC. Because these pulmonary alterations occurred too late in the progression of HF, the incipient physiological mechanism that causes diaphragm atrophy cannot be attributed to lung remodeling and reduced compliance.

Mancini *et al.* demonstrated that patients with HF have significantly elevated TTI at rest and during exercise (*14*). The elevated TTI results from increases in resting P_I and decreases in P_{Imax}, without changes in duty cycle (T_I/T_{total}) or inspiratory time (T_I). Thus, we investigated changes in resting P_I and ventilatory drive throughout development of pressure overload–induced HF in mice. Consistent with the clinical findings, at all time points, resting P_I was elevated (Fig. 4, A and B) because of an increase in ventilatory drive (P_I/T_I; Fig. 4C) with no changes in duty cycle or T_I (table S1). Because increased resting P_I and ventilatory overdrive preceded the onset of diaphragm atrophy, identifying their causes would provide insight into the cause of atrophy.

The cause of elevated resting P_I is unresolved in humans. We measured 24-hour CO_2 and O_2 production in 2-week TAC mice, finding both parameters significantly, yet proportionally, decreased compared to sham (table S1). We also found similar blood lactate levels in sham and 2-week TAC mice (6.5 versus 6.7 mM; $P = 0.545$, two-tailed Student's t test). These results are consistent with clinical data suggesting that ventilatory overdrive and P_I are elevated independent of chemical drive (that is, CO_2, H^+, and O_2) (*34*).

Up to this point, we have shown that the physiological mechanism for the cause of atrophy is a stress that specifically affects the diaphragm and involves neither changes in lung mechanics nor chemical drive. These findings suggest the possibility that a stimulatory neurohormonal mechanism might cause the increase in resting P_I observed in mice with pressure overload–induced HF. This rationale is supported by previous work that demonstrated a case in which hormones (estrogen and progesterone) can increase ventilatory drive (*35*, *36*) independent of chemical drive. In HF, neurohormonal dysfunction is classically associated with increased catecholamines and

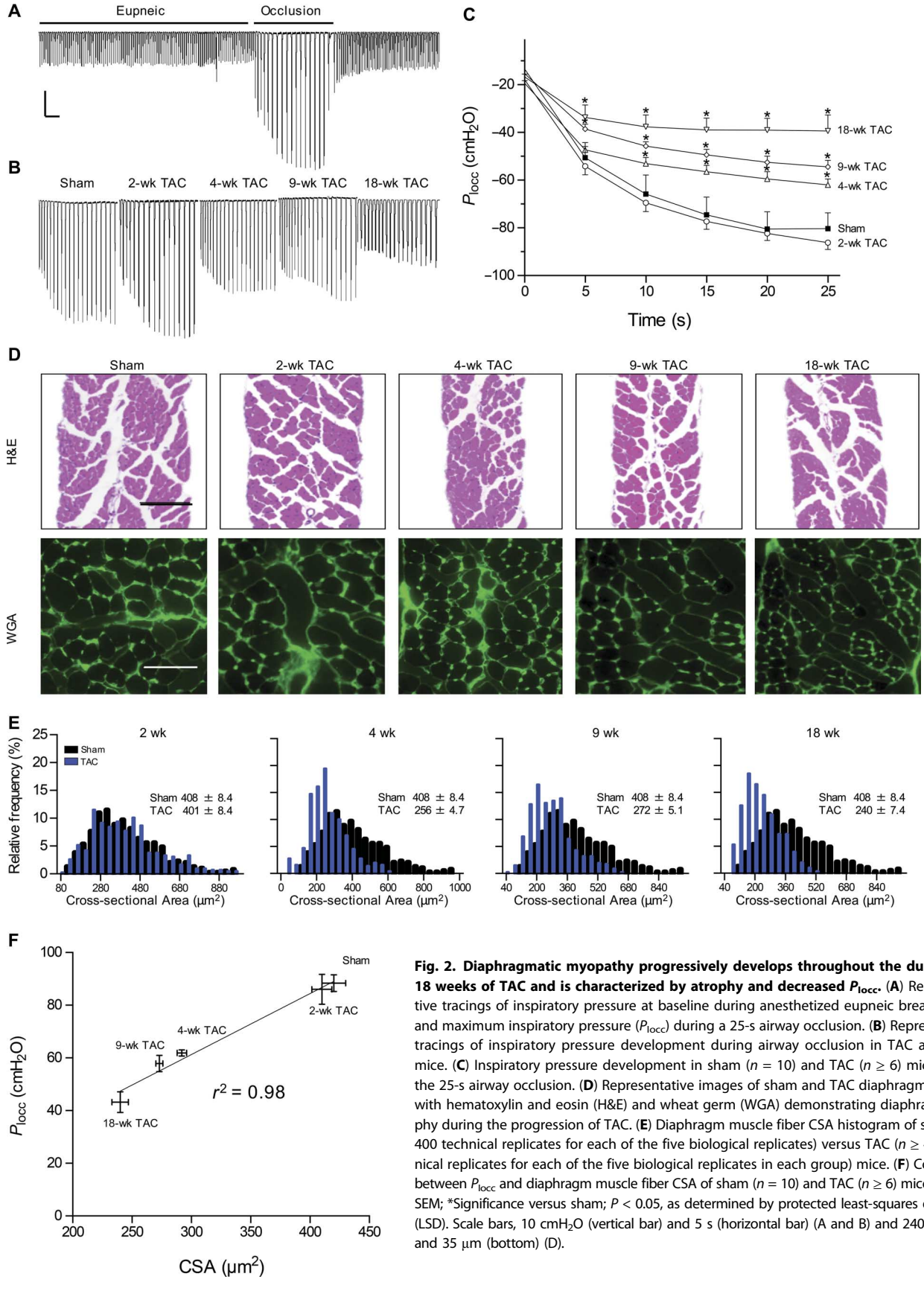

Fig. 2. Diaphragmatic myopathy progressively develops throughout the duration of 18 weeks of TAC and is characterized by atrophy and decreased P_{locc}. (**A**) Representative tracings of inspiratory pressure at baseline during anesthetized eupneic breathing (P_I) and maximum inspiratory pressure (P_{locc}) during a 25-s airway occlusion. (**B**) Representative tracings of inspiratory pressure development during airway occlusion in TAC and sham mice. (**C**) Inspiratory pressure development in sham (n = 10) and TAC ($n \geq 6$) mice during the 25-s airway occlusion. (**D**) Representative images of sham and TAC diaphragms stained with hematoxylin and eosin (H&E) and wheat germ (WGA) demonstrating diaphragm atrophy during the progression of TAC. (**E**) Diaphragm muscle fiber CSA histogram of sham ($n \geq$ 400 technical replicates for each of the five biological replicates) versus TAC ($n \geq$ 400 technical replicates for each of the five biological replicates in each group) mice. (**F**) Correlation between P_{locc} and diaphragm muscle fiber CSA of sham (n = 10) and TAC ($n \geq 6$) mice. Mean ± SEM; *Significance versus sham; $P < 0.05$, as determined by protected least-squares difference (LSD). Scale bars, 10 cmH$_2$O (vertical bar) and 5 s (horizontal bar) (A and B) and 240 μm (top) and 35 μm (bottom) (D).

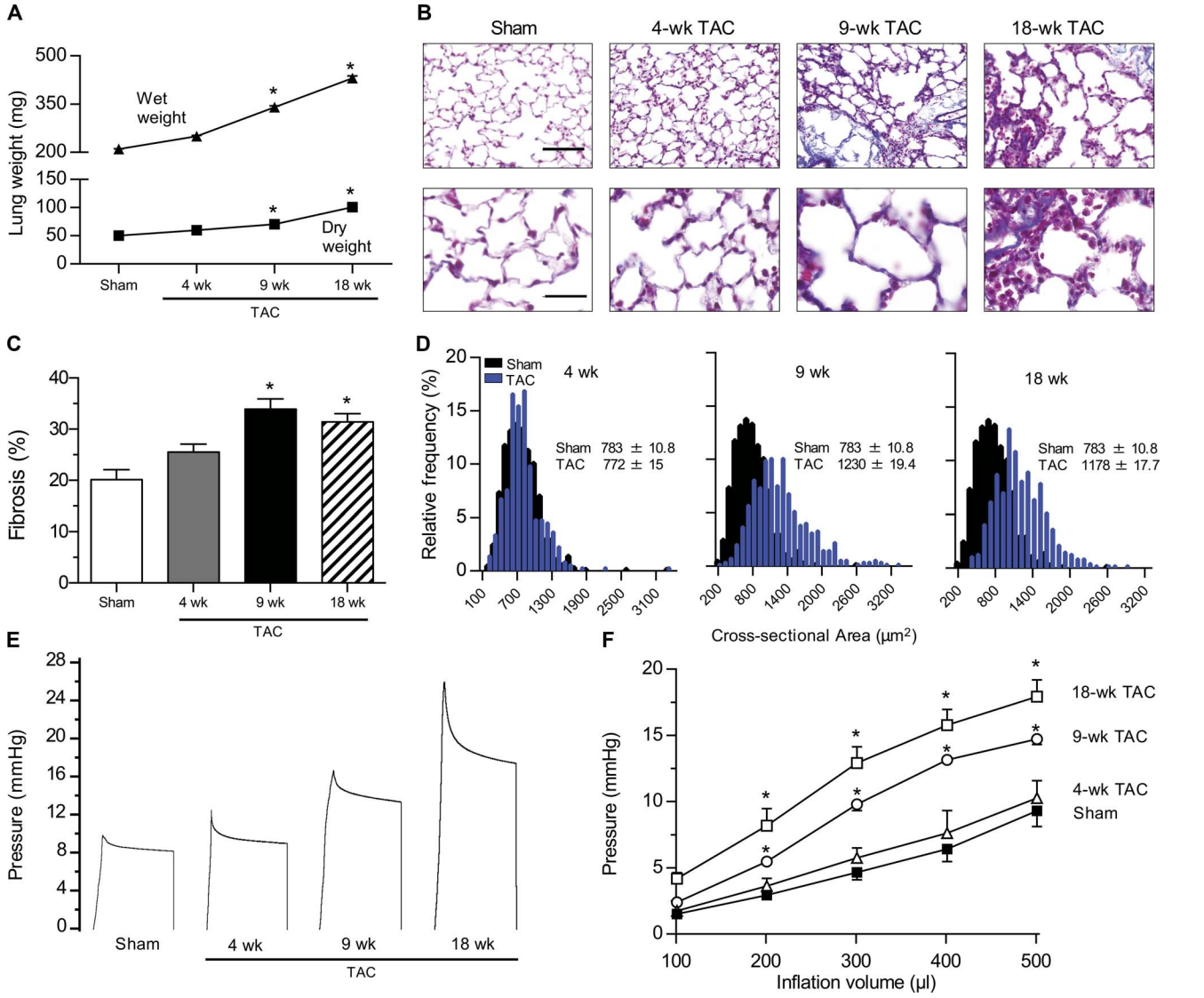

Fig. 3. TAC induces progressive and profound lung remodeling that reduces dynamic lung compliance in late-stage TAC. (**A**) Lung wet and dry weights of sham and TAC mice. (**B**) Representative images of lung tissue stained with Gomori's trichrome. (**C**) Interstitial/alveolar pulmonary fibrosis ($n = 5$). (**D**) Histogram of alveolar CSA in sham ($n = 5$) and TAC ($n = 5$) mice. (**E**) Representative raw pressure tracings during 200 μl of lung inflation for the measurement of dynamic lung compliance in sham and TAC mice. (**F**) Dynamic lung compliance curves of sham ($n = 4$) and TAC ($n = 4$ for each group) mice. Mean ± SEM; *Significance versus sham; $P < 0.05$, as determined by protected LSD. Scale bars, 30 μm (top) and 15 μm (bottom) (B).

activation of the renin-angiotensin-aldosterone system (RAAS). As such, we sought to investigate the role of these hormone systems in the stimulation of ventilatory drive. In 2-week TAC mice, we acutely administered either an angiotensin-converting enzyme (ACE) inhibitor (captopril) or a nonselective β-ADR blocker (propranolol) to systemically attenuate ANGII or β-ADR signaling. Acute administration of either drug normalized P_I in 2-week TAC mice to sham levels (Fig. 4D), implicating ANGII and β-ADR signaling as ventilatory stimuli in HF.

To resolve whether ANGII and β-ADR signaling increases ventilatory drive as a result of HF or whether it is an innate mechanism, we infused ANGII or isoproterenol (a nonselective β-ADR agonist) into healthy mice. Both hormones spurred a dose-dependent increase in P_I (Fig. 4E) and ventilatory drive. It was not clear why captopril and propranolol decreased P_I in 2-week TAC mice with equal efficacy. However, ANGII and β-ADR receptors exhibit cross-talk and are transinhibitory in the heart (*37*). β-ADR blockade inhibits ANGII-mediated signaling and vice versa. To test for a transinhibitory effect of ANGII and β-ADR blockade on ventilatory drive, we infused ANGII with propranolol or isoproterenol with captopril. This experiment abolished the effects of either hormone in the presence of their transinhibitors (Fig. 4E). This indicates a functional codependent mechanism between the ANGII and β-ADR systems to regulate ventilatory drive. Because ANGII is a potent initiator of smooth muscle contraction, we wanted to ensure that the resultant increase in P_I was not an indirect consequence of airway smooth muscle constriction. During intravenous ANGII infusion, we simultaneously measured airway pressure and neural drive [that is, by diaphragm electromyography (EMG)] in healthy open-chested, anesthetized mice during mechanical ventilation. This technique provides a means to separate neural drive from increased airway resistance

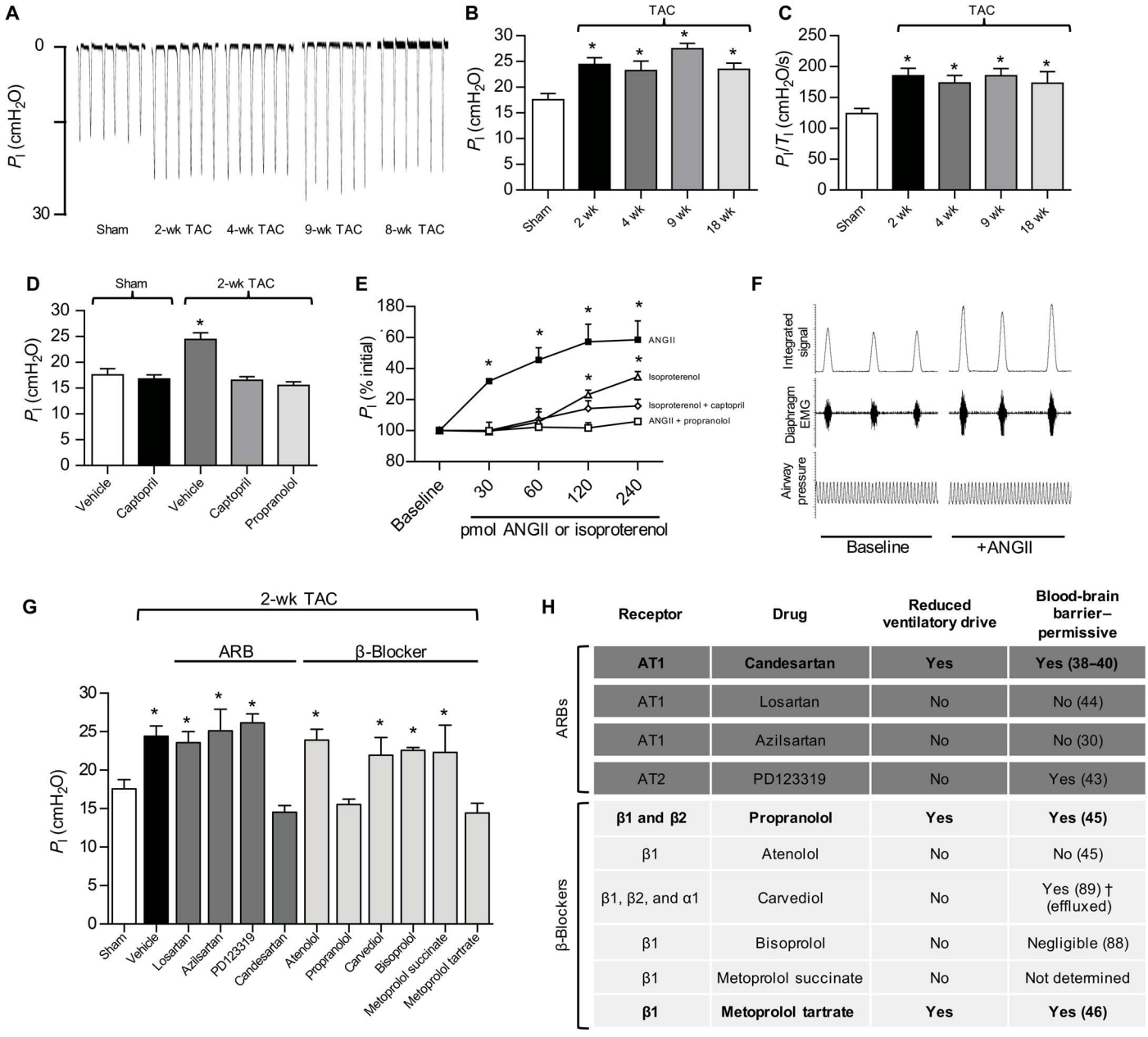

	Receptor	Drug	Reduced ventilatory drive	Blood-brain barrier–permissive
ARBs	**AT1**	**Candesartan**	**Yes**	**Yes (38–40)**
	AT1	Losartan	No	No (44)
	AT1	Azilsartan	No	No (30)
	AT2	PD123319	No	Yes (43)
β-Blockers	**β1 and β2**	**Propranolol**	**Yes**	**Yes (45)**
	β1	Atenolol	No	No (45)
	β1, β2, and α1	Carvediol	No	Yes (89) † (effluxed)
	β1	Bisoprolol	No	Negligible (88)
	β1	Metoprolol succinate	No	Not determined
	β1	**Metoprolol tartrate**	**Yes**	**Yes (46)**

Fig. 4. ANGII and β-ADR codependent signaling stimulates neural ventilatory drive that is only normalized by antagonists that cross the BBB. (**A**) Representative tracings of inspiratory pressure during anesthetized breathing at rest in sham and TAC mice. (**B**) Inspiratory pressure (PI) and (**C**) ventilatory drive (PI/TI) during anesthetized breathing in sham and TAC mice. (**D**) Inspiratory pressure of sham and TAC mice following acute treatment with captopril or propranolol. (**E**) Inspiratory pressure measured during the infusion of ANGII or isoproterenol in the presence or absence of captopril or propranolol ($n = 4$ for each combination). (**F**) Representative tracing of diaphragmatic EMG and airway pressure during the infusion of ANGII. (**G**) Inspiratory pressure in sham and 2-week TAC mice in the presence or absence of ANGII or β-ADR receptor blockers ($n = 8$ for each combination). (**H**) Chart indicating the ability of various ANGII and β-ADR receptor blockers to cross the BBB. Mean ± SEM; *Significance versus sham; $P < 0.05$, as determined by protected LSD. †Carvediol is rapidly effluxed and does not accumulate within the brain.

due to constriction. Infusion of ANGII increased diaphragm EMG but not airway pressure (Fig. 4F). This confirmed that increased P_I was not the indirect consequence of airway constriction but rather the result of direct neural stimulation of ventilation caused by ANGII and β-ADR signaling.

In HF, ANGII is a key mediator of the RAAS and a partial regulator of catecholamine production. These effects are mediated principally through AT1 and AT2 receptors, which are located both centrally (*38*–*41*) and peripherally (*41*, *42*). Likewise, ventilation is also regulated by central and peripheral mechanisms. To ascertain if the ventilatory stimuli of ANGII and β-ADR signaling were centrally or peripherally mediated, we tested the effects of angiotensin receptor antagonists that were either blood-brain barrier (BBB)–permeant [candesartan (*38*–*40*) and PD123319 (*43*)] or BBB-impermeant [losartan (*44*) and azilsartan (*30*)]. P_I was unchanged in 2-week TAC mice after administration of losartan (AT1 antagonist), azilsartan

(AT1 antagonist), or PD123319 (AT2 antagonist) (Fig. 4G). However, BBB-permeant candesartan normalized P_I to sham levels (Fig. 4G), suggesting a centrally mediated mechanism. To confirm that ventilatory overdrive was centrally mediated, we tested the transinhibitory mechanism using selectively permeant β-blockers. Indeed, atenolol [BBB-impermeant (*45*)] did not display a propranolol-comparable reducing effect [BBB-permeant (*45*)] (Fig. 4G) on ventilatory overdrive. Clinically, atenolol and propranolol are generally prescribed for the treatment of hypertension, whereas carvedilol, metoprolol, and bisoprolol are frontline medications recommended for HF patients. Further corroborating our findings, only the BBB-permeant metoprolol (*46*), in its fast-release formulation, was effective at reducing ventilatory overdrive in 2-week TAC mice (Fig. 4G). Therefore, our results suggest that the ventilatory stimulus that promotes increased resting P_I and ventilatory overdrive is mediated via receptors that are contained within the BBB (Fig. 4H); this is a critical finding because most pharmacological agents used to treat hypertension and HF in an outpatient setting do not cross the BBB.

Chronic ventilatory overdrive causes enhanced diaphragm function followed by atrophy

Having identified the cause of ventilatory overdrive, we next investigated the mechanism of diaphragmatic atrophy. The earliest indication that HF had affected diaphragm function in our model was enhanced in vitro force production at 2 weeks of TAC (fig. S2). Catecholamines are overactive in HF and, via β-ADR, act as potent cardiac inotropes, but their effects on the diaphragm are unknown. Thus, we investigated whether acute β-ADR stimulation was the cause for increased in vitro function. To test this, we measured in vitro function during repeated nonfatiguing submaximal electrical stimulations before and after incubation with a β-ADR agonist, isoproterenol (Fig. 5, A and B). Incubation had no effect on contractility or passive

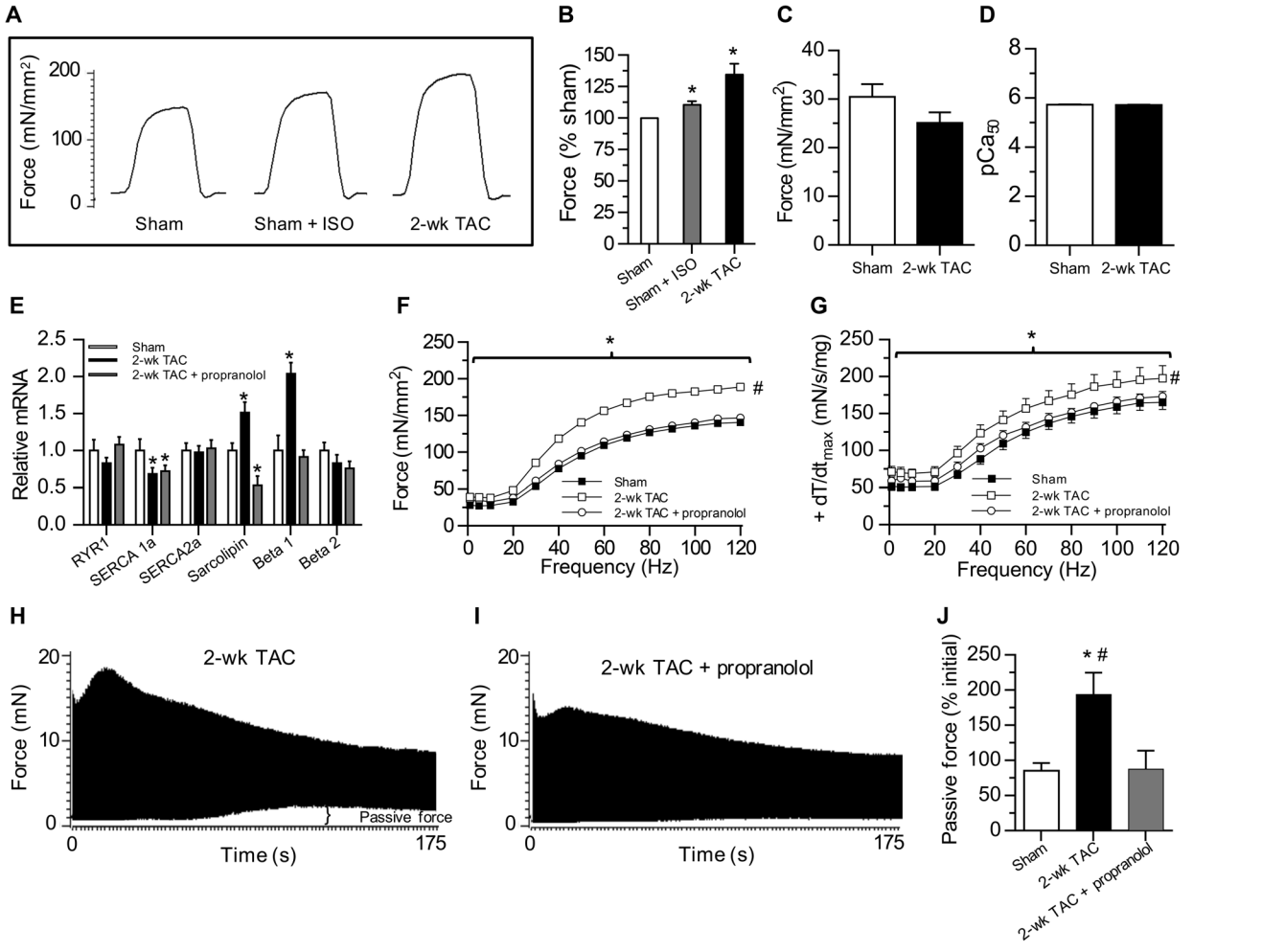

Fig. 5. Chronic β-ADR blockade normalizes diaphragm in vitro function that is not explained by acute β-ADR stimulation or alterations in myofilament function. (**A**) Raw tracings of in vitro tetanic contraction from sham, sham + isoproterenol (ISO), and 2-week TAC diaphragm. (**B**) Maximal in vitro force production of sham (n = 10), sham + isoproterenol (n = 6), and 2-week TAC diaphragm (n = 14). (**C**) Diaphragm myofilament force production and (**D**) calcium sensitivity (pCA_{50}) of sham (n = 17) and 2-week TAC (n = 19) mice. (**E**) Relative mRNA expression in sham, 2-week TAC, and 2-week TAC + propranolol mice (n = 3 technical replicates for each of the five biological replicates in each group). (**F**) Peak force production and (**G**) maximum rate of force production $+dT/dt_{max}$ during force-frequency protocol in sham (n = 12), 2-week TAC (n = 14), and 2-week TAC + propranolol (n = 7) mice. Representative tracings of in vitro fatigue protocol in (**H**) 2-week TAC and (**I**) 2-week TAC + propranolol diaphragms. (**J**) Maximum passive force development of sham (n = 12), 2-week TAC (n = 14), and 2-week TAC + propranolol (n = 7) diaphragms during in vitro fatiguing stimulations. All mRNAs are expressed relative to the housekeeping gene *Hmbs* (hydroxymethylbilane synthase). Mean ± SEM; *Significance versus sham; $P < 0.05$, as determined by protected LSD. #Significance versus 2-week TAC + propranolol; $P < 0.05$, as determined by protected LSD.

baseline force but marginally increased peak force production by ~9% (Fig. 5B); subsequent additions of isoproterenol did not cause further changes. Although acute β-ADR activation slightly increased in vitro force, it was significantly less than that observed in 2-week TAC diaphragm, establishing that additional mechanisms remain to be elucidated.

In cardiac muscle, β-ADR activation leads to both acute and chronic changes in cardiac function, specifically by altering myofilament proteins (*47*–*49*) and calcium handling (*50*, *51*). Whereas the effects of β-ADR stimulation on cardiac myofilament function are well studied, the effects of these agents on skeletal myofilament function are unknown. Therefore, to determine whether chronic β-ADR activation increased force production by altering myofilament function, we assessed force production and myofilament Ca^{2+} sensitivity of 2-week TAC skinned diaphragm myofilaments. Maximum myofilament force production (Fig. 5C) and sensitivity (as indicated by pCa_{50}; Fig. 5D) were unchanged from sham. These results were unexpected because in vitro force production was increased by ~35% in 2-week TAC diaphragms (Fig. 5B and fig. S2), and we showed previously that the passive force of a single skinned diaphragm fiber is reduced after 2 weeks of TAC as compared to sham mice (*52*). Because the increased in vitro force production did not have parallel increases in either myofilament sensitivity or force production, the causal mechanism likely resides with enhanced Ca^{2+} handling. The increase in baseline passive force production during fatiguing stimulations (fig. S2) was consistent with alterations in Ca^{2+} handling. Thus, we sought to investigate the key components of the Ca^{2+} handling system in diaphragm tissue by quantitative polymerase chain reaction (qPCR) analysis. The diaphragm from 2-week TAC mice revealed a 30% reduction in *Serca1a* and a 50% increase in sarcolipin, coupled with a doubling of β-ADR subtype 1 expression (Fig. 5E). These results are consistent with reduced Ca^{2+} reuptake because *Serca1a* is the predominant Ca^{2+}-ATPase isoform in skeletal muscle and sarcolipin acts to inhibit *Serca1a* activity (*53*). An analogous molecular profile is observed in cardiac tissue from HF mouse models, in which altered Ca^{2+} handling also exists (*53*) and often causes endoplasmic reticulum (ER) stress. Hence, up-regulation of sarcolipin and down-regulation of *Serca1a* suggest that Ca^{2+} reuptake is reduced by 2 weeks of TAC, resulting in the accumulation of cytosolic Ca^{2+} and translating to an increase in peak (fig. S2) and passive (fig. S2) in vitro force production. Although acute β-ADR stimulation did not explain the increased in vitro force production observed at 2 weeks of TAC (Fig. 5, A and B), this does not exclude persistent β-ADR–induced ventilatory overdrive as the mechanism.

We next treated a subset of TAC mice with a β-ADR blocker, propranolol, to investigate whether persistent β-ADR–induced ventilatory overdrive resulted in enhanced diaphragmatic function. Propranolol treatment for 2 weeks normalized ventilatory overdrive and ameliorated the effects of TAC on in vitro diaphragmatic function (Fig. 5, F to J). Normalization of diaphragmatic function was also associated with a reduction in sarcolipin and *Beta 1* (β-ADR subtype 1) mRNA, as compared to the untreated 2-week TAC group (Fig. 5E). Collectively, these data demonstrated that enhanced in vitro diaphragmatic force production after 2 weeks of TAC was neither the result of increased myofilament force production nor the result of acute β-ADR stimulation on the muscle. Rather, persistent β-ADR–induced ventilatory overdrive resulted in altered Ca^{2+} handling, as indicated by elevated passive and peak force production. Indices of systolic and diastolic cardiac function in the 2-week TAC, propranolol-treated group were comparable to the untreated group (table S3). Therefore, the normalization of diaphragm function after chronic (that is, 2 weeks) propranolol treatment was not the result of treating the cardiac dysfunction. Propranolol's ameliorative effects on cardiac hemodynamic dysfunction are negligible in early TAC (table S3).

Having accounted for the enhanced in vitro force production as a consequence of persistent β-ADR–induced ventilatory overdrive, we next explored whether this was also the mechanism for subsequent atrophy. To exclude the possibility that peripheral β-ADR activation played a role in the development of diaphragmatic atrophy, we compared 4 weeks of chronic treatment with either atenolol (peripheral only) or propranolol (peripheral and central). Four weeks of chronic propranolol, but not atenolol, treatment prevented the development of diaphragm atrophy (CSA; Fig. 6, A to C) and preserved inspiratory strength (P_{Iocc}; Fig. 6D). We also treated another subset of mice throughout the duration of 9-week TAC with propranolol, again, with no evidence of diaphragm atrophy. Thus, chronic propranolol treatment did not delay, but rather prevented, the development of atrophy in HF, affirming chronic central β-ADR stimulation as the causative mechanism.

Muscle fiber size (that is, CSA) is maintained by a homeostatic balance between protein synthesis and degradation. Diaphragm atrophy can occur as a result of cellular degeneration, enhanced protein degradation, or impaired protein synthesis. To elucidate the molecular mechanism of atrophy, we profiled 4-week TAC diaphragms for genetic markers of apoptosis (Fig. 6E), autophagy (Fig. 6F), protein degradation (Fig. 6G), regeneration and repair (Fig. 6H), and ER stress and unfolded protein response (Fig. 6I). There was no evidence of apoptosis or autophagy. Key markers of skeletal muscle degradation (*Foxo1*, *Foxo3*, *Foxo4*, and *Murf-1*) were all down-regulated, with the exception of atrogin, a ubiquitin protein ligase (Fig. 6G). Furthermore, despite profound atrophy, in vitro diaphragmatic force production and contractility in 4-week TAC mice were not reduced, a finding incongruent with muscle proteolysis. In profiling gene expression for muscle regeneration and repair, myogenin and *Myf5*, both markers of skeletal muscle regeneration (Fig. 6H), were significantly elevated. We also demonstrated a significant increase in the expression of actin and the embryonic isoform of myosin heavy chain (*MHC-Emb*; Fig. 6H). Thus, the prevailing diaphragmatic phenotype was one of atrophy, whereas the molecular expression profile favored muscle regeneration.

ER stress and the unfolded protein response can uncouple mRNA and protein synthesis (*54*); thus, we investigated the expression of genes associated with these processes in diaphragms from sham and 4-week TAC mice (Fig. 6I). qPCR analysis revealed increased expression of *heme-oxygenase 1*, *Perk, XBp1,* and *XBp1* splice variant—indicative of ER stress (*55*–*57*) in 4-week TAC diaphragms (Fig. 6I). *Perk*, an ER-transmembrane protein kinase that couples ER stress to the inhibition of protein translation, was increased by about twofold (Fig. 6I). The downstream target of *Perk*, eukaryotic translation initiation factor 2α (EIF2α), inhibits the initiation of protein translation when phosphorylated by *Perk* and was unchanged (Fig. 6I). Furthermore, expression of *Chop*, which promotes protein synthesis by dephosphorylating EIF2α, was significantly reduced (Fig. 6I). Together, the unfolded protein response molecular profile suggested a net increase in EIF2α phosphorylation as the molecular mechanism causing diaphragm atrophy. This molecular mechanism was strengthened by being treatable with propranolol but not atenolol (Fig. 6J and fig. S6) and was further corroborated in the absence of TAC (fig. S5). For further confirmation at the protein level, we examined total and phospho–Ser^{51}-EIF2α levels in the diaphragm from 4-week TAC mice. Although EIF2α protein

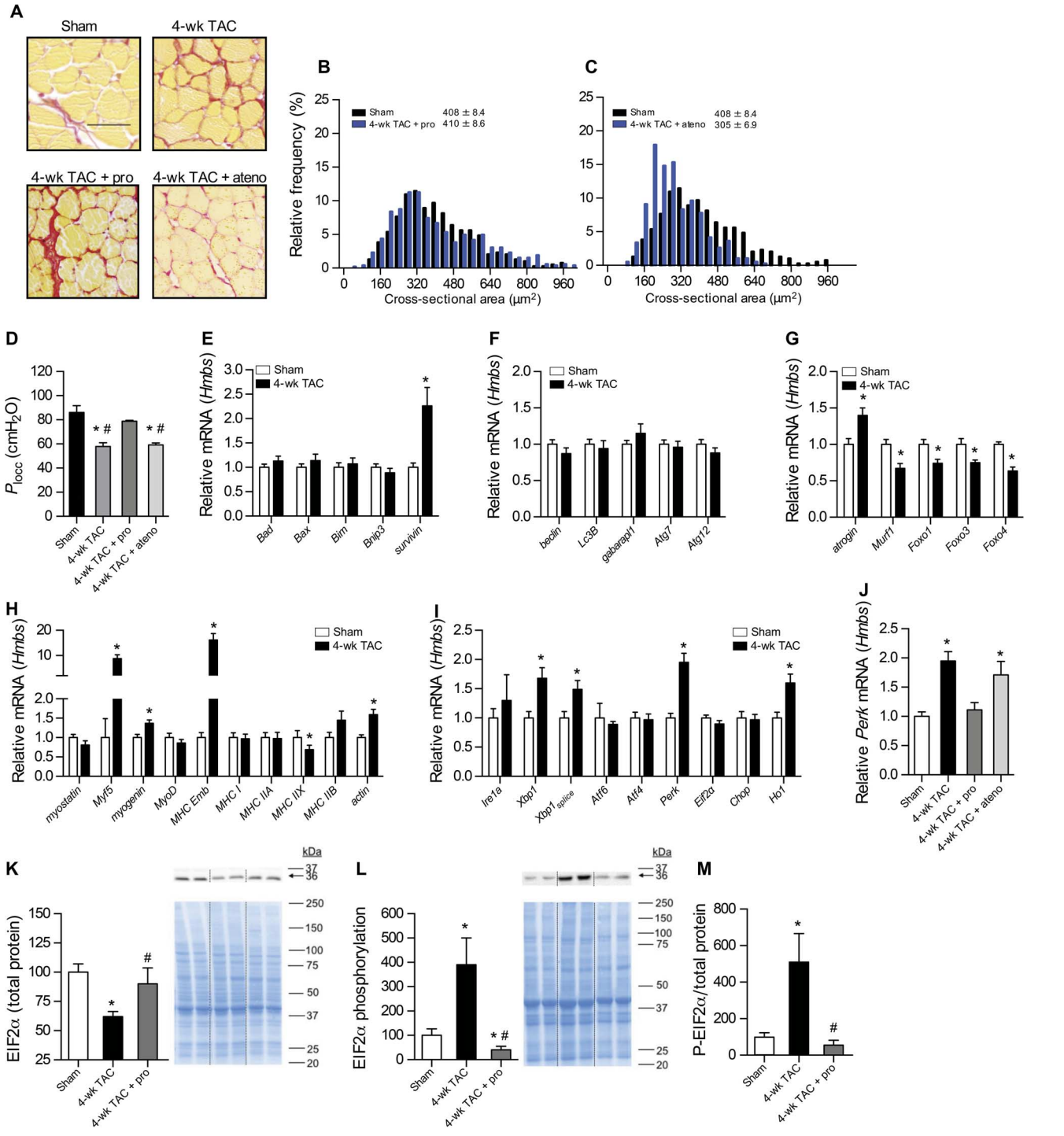

Fig. 6. BBB-permeant β-blockers ameliorate diaphragm atrophy, restore inspiratory strength, and normalize EIF2α phosphorylation and relative *Perk* expression in TAC mice. (**A**) Representative cross-sectional images of diaphragm from sham, 4-week TAC, 4-week TAC + propranolol (pro), and 4-week TAC + atenolol (ateno) stained with picrosirius red. (**B**) Diaphragm muscle fiber CSA histogram of sham ($n \geq 400$ technical replicates for each of the five biological replicates) versus 4-week TAC + propranolol mice ($n \geq 400$ technical replicates for each of the five biological replicates) or (**C**) 4-week TAC + atenolol mice ($n \geq 400$ technical replicates for each of the five biological replicates). (**D**) Maximal inspiratory pressure during a 25-s airway occlusion in sham ($n = 10$), 4-week TAC ($n = 8$), 4-week TAC + propranolol ($n = 6$), and 4-week TAC + atenolol ($n = 5$) mice. (**E** to **I**) Relative diaphragm mRNA expression of key gene markers involved in (E) apoptosis, (F) autophagy, (G) degradation, (H) regeneration, and (I) the unfolded protein response in sham and 4-week TAC mice ($n = 3$ technical replicates for each of the five biological replicates in each group). (**J**) Relative diaphragm *Perk* mRNA expression in sham, 4-week TAC, 4-week TAC + propranolol, or atenolol-treated mice ($n = 3$ technical replicates for each of the five biological replicates in each group). (**K**) Diaphragm total protein content, (**L**) phosphorylation, and (**M**) protein/phosphorylation ratio of sham ($n = 5$), 4-week TAC ($n = 5$), and 4-week TAC + propranolol ($n = 5$) with MemCode stains and Western blots. All mRNA are expressed relative to the housekeeping gene *Hmbs*. Mean ± SEM; *Significance versus sham. #Significance versus 4-week TAC; $P < 0.05$, as determined by protected LSD. Scale bar, 50 μm (A).

levels were reduced (Fig. 6K), absolute levels (Fig. 6L) and the relative ratio (Fig. 6M) levels of phospho-Ser^{51} were significantly increased, about four- and fivefold, respectively. Furthermore, 4 weeks of propranolol treatment normalized *Perk* expression and EIF2α protein and phospho-Ser^{51} levels (Fig. 6, J to M) along with normalization of diaphragmatic CSA and preservation of inspiratory strength (P_{Iocc}; Fig. 6D). Collectively, gene expression analysis revealed that diaphragm atrophy, preventable with chronic propranolol (but not atenolol) treatment, was the result of impaired protein synthesis induced by increased *Perk* expression and EIF2α Ser^{51} phosphorylation. Together, our data show that, in HF, a central neurohormonal increase in ventilatory drive acutely enhances diaphragmatic function yet, when chronically activated without resolution, inhibits protein synthesis, causing diaphragmatic atrophy and weakness.

DISCUSSION

Here, we show that the development of respiratory dysfunction occurs in three evolving stages in HF, which accumulate as a neuroinspiratory myopulmonary syndrome (Fig. 7). We have discovered a neurohormonal mechanism that increases ventilatory drive, resulting in a chronically higher work-of-breathing in HF, independent of changes in lung mechanics or the presence of pulmonary edema. Subsequent to enhanced diaphragmatic contractility, atrophy—the incipient cause of diaphragmatic weakness—developed as a consequence of chronic ventilatory/diaphragm overdrive, leading to *Perk* up-regulation and downstream phosphorylation and inhibition of EIF2α. Pathological lung remodeling occurred late in the progression of HF, resulting in fibrotic deposition and resultant restrictive lung function. Critically, only ANGII and β-ADR blockers—which are capable of crossing the BBB—were effective in normalizing ventilatory drive and alleviating diaphragmatic weakness, independent of improvement in cardiac function. Thus, translational pharmacology will require specific consideration in drug selection so as to target both the respiratory and cardiovascular dysfunction in HF patients to improve outcome and quality of life.

In contrast to peripheral muscle, little is known about diaphragmatic alterations in HF, probably because most studies have primarily examined end stages of the disease. Consequently, no information on the causation and/or progression of the pathophysiological mechanisms has been reported. Our objective was to investigate the incipient and sequential mechanisms causing diaphragmatic dysfunction. HF-induced atrophy was first and foremost observed at the level of the diaphragm by 4 weeks of TAC and progressed by 18 weeks in our experimental model. The strong correlation between diaphragmatic atrophy and maximal inspiratory pressure generation establishes that the initial cause of diaphragm weakness in HF is solely attributable to the atrophy. In contrast to other models (*17*–*19*, *21*, *58*), such as myocardial infarction and ventricular pacing, we found no evidence of in vitro diaphragmatic dysfunction at the time points we investigated. Because our study focused on early HF, atrophy likely precedes the development of any intrinsic contractile deficit.

Here, we show a codependent mechanism between β-ADR and ANGII signaling that increases neural ventilatory drive to induce a state of chronic diaphragmatic hyperactivity. Blockade of this ventilatory overdrive prevented the development of diaphragmatic atrophy and preserved inspiratory muscle strength. Systemic β-ADR agonists typically stimulate skeletal muscle hypertrophy (*59*). The observation that gastrocnemius and soleus (peripheral muscles in the limbs) showed no evidence of atrophy indicates that atrophy first develops at the level of the diaphragm. Had atrophy been the result of direct β-ADR stimulation on the muscle, we would expect (i) a parallel effect in diaphragm and peripheral muscles and (ii) that atenolol would block HF-induced diaphragm atrophy, which it did not. However, limb muscle atrophy is an important feature of HF-induced exercise intolerance and likely appears later in our model. In contrast to limb muscles, the diaphragm is subjected to sustained hyperactivity without rest, resulting in the rapid development of atrophy. Whereas the increase in resting pressure generation (at all time points) appeared modest, it underrepresented the actual increase in muscle activity. Because the airway is not occluded, increases in pressure generation are dissipated in airflow. Thus, even a modest increase in resting pressure generation reflected a significant increase in muscle activity.

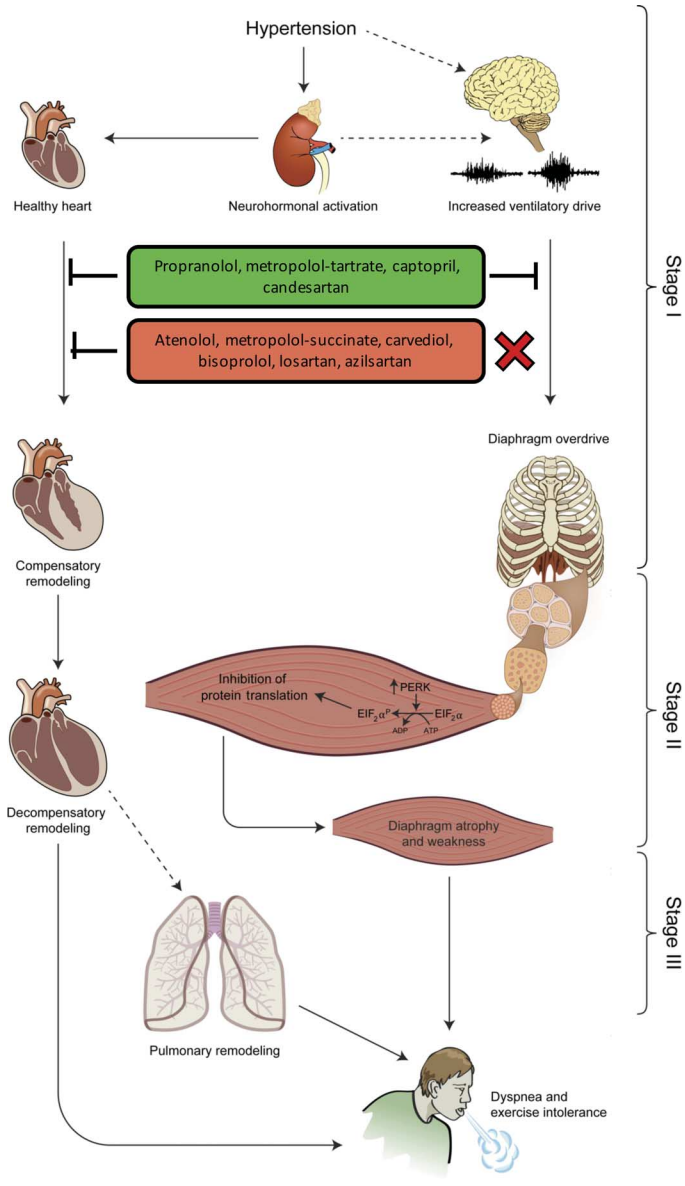

Fig. 7. Heart failure–induced ventilatory overdrive triggers the development of diaphragm atrophy and weakness independent of pulmonary edema or lung remodeling.

Chronically elevated contractile activity stimulates the proteasome pathway in skeletal muscle, leading to protein degradation and atrophy (*60*). However, despite the profound atrophy observed, we found no evidence of protein degradation in our model. Protein translation is also attenuated in response to heightened contractile activity (*61*, *62*) without the activation of degradation pathways, which aligns with our findings. The precise mechanism(s) responsible for reducing protein translation during heightened contractile activity are not fully understood. One possibility is the activation of the unfolded protein response due to ER stress (*63*). The unfolded protein response is composed of three branches: (i) *Atf6*, (ii) *Ire1*, and (iii) *Perk*—of which, *Perk* activation inhibits protein translation (*55*). In our model, up-regulation of *Perk* expression was positively associated with the development of atrophy. Nonetheless, chronic activation of *Perk* can be either cytoprotective (*64*–*66*) and/or apoptotic (*66*, *67*) under different conditions. ER stress can activate the transcription factor CHOP, which mediates apoptosis. We found no histological or molecular evidence of skeletal muscle apoptosis and no change in *Chop* expression, suggesting limited activation of the ER stress response. This is in agreement with other reports that, in the absence of *Chop* activation, ER stress activates *Perk* (*68*, *69*) and inhibits *Atf6* and *Ire1* signaling (*68*, *69*), which would support our findings. Although this is controversial, current evidence indicates that the magnitude and duration of ER stress determine whether chronic *Perk* activation results in apoptosis or cell survival (*68*, *69*). This reconciles our observation of diaphragm atrophy in the absence of apoptosis or protein degradation. The downstream evidence for protein hyperphosphorylation of EIF2α confirms that atrophy was the result of arrested protein translation. This explains why an expression profile favoring myocyte renewal and regeneration failed to deliver any effect. Typically, ER stress causes activation of *Atf6*, *Ire1*, and *Perk* of the unfolded protein response and their downstream pathways. However, we observed hyperphosphorylation of EIF2α that was associated with increased *Perk* mRNA expression rather than activation. Whether this hyperphosphorylation of EIF2α is solely the result of increased *Perk* levels or also reflects, at least in part, activation of the ER stress response remains to be investigated. The molecular mechanism of diaphragm atrophy was due to increased *Perk* expression with resultant hyperphosphorylation of EIF2α, thus limiting protein translation.

Ventilatory drive is largely regulated by CO_2, H^+, and, to a lesser extent, hypoxia. Although it is atypical to ascribe alterations of ventilatory drive to hormonal regulation, we are not the first to discover that such hormonal modulation can occur. Estrogen and progesterone increase the sensitivity of the central chemoreflex to CO_2 during the luteal phase and pregnancy (*35*), resulting in hypocapnia. Moreover, estrogen- and progesterone-mediated ventilatory drive increases resting P_I independent of the duty cycle (*36*), similar to what we report here with ANGII and catecholamines. Coincidently, estrogen and progesterone activate E2 receptors in areas behind the BBB, such as the hypothalamus, ventromedial medulla, and solitary nucleus, all sites with localized ANGII receptors (mainly AT1) (*70*–*73*). Future work is necessary to identify the neuroanatomical receptor density for ANGII and catecholamines and other receptors that are responsible for ventilatory drive modulation.

Our direct infusion and inhibitor experiments indicate that central ventilatory drive is elicited by both ANGII and catecholamines in healthy and TAC animals. Whereas catecholamine and ANGII permissiveness to cross the BBB remains controversial, our data support the contention for an AT1/β-ADR–mediated elevation in central ventilatory drive because only BBB-permeant AT1 and β-ADR blockers were capable of reducing ventilatory drive.

Our findings are relevant to the pathophysiology and treatment of HF, specifically surrounding the use of ARBs and β-ADR blockers. Similar to ACE inhibitors (such as captopril), ARBs reduce blood pressure and are used in the treatment of hypertension. ACE inhibitors and ARB are both effective at reducing blood pressure (*74*). However, unlike ACE inhibitors, ARBs are receptor-specific (AT1 versus AT2) and thus confer fewer side effects than ACE inhibitors (*74*). Despite belonging to the same drug class, ARBs are variable in their pharmacodynamic and pharmacokinetic characteristics (*30*). Although candesartan and losartan similarly reduced blood pressure, in a study of 14,100 hypertensive patients, total cardiovascular disease, HF, and cardiac arrhythmias were markedly lower in patients who were prescribed candesartan (*31*); the reason for this discrepancy remains unclear.

We found that only candesartan normalized ventilatory drive, and we attribute this to its ability to cross the BBB. Thus, an obvious question is whether the additional benefits of candesartan observed clinically (*31*) reflect normalization of ventilatory drive via blockade of central AT1 receptors. This notion is not unreasonable because acute and chronic respiratory loads cause cardiac injury (*75*–*78*), highlighting the integration of respiratory and cardiac pathophysiology. Lipophilic β-blockers (such as propranolol) have shown lower rates of mortality in patients with coronary heart disease, as compared to hydrophilic agents (such as atenolol) that are unable to cross the BBB (*79*). Similar to the results using ARBs, only BBB-permeant therapeutics were effective in treating ventilatory overdrive. Thus, the ability for certain lipophilic β-blockers to reduce ventilatory drive could be a factor in determining clinical outcomes. β-Blockers have shown variability in modulating clinical outcomes. Literature evidence on this point both supports (*80*–*86*) and refutes (*87*–*91*) a difference in clinical outcome between different β-blockers. As an example, metoprolol (meta-analysis included studies with both succinate and tartrate) is superior to carvedilol and bisoprolol [negligible BBB permeability (*92*)] in reducing sudden death (*82*). In contrast, all-cause mortality was reduced with carvedilol versus metoprolol tartrate; yet, neither mortality nor hospitalizations were significantly different between carvedilol and metoprolol succinate (*89*). Although carvedilol is BBB-permeant, it is effluxed by P-glycoprotein-1 so that it does not accumulate in the brain (*93*). Metoprolol tartrate crosses the BBB (*46*), but the ability of metoprolol succinate to penetrate the BBB is unclear. Here, only metoprolol tartrate and propranolol effectively reduced ventilatory overdrive. Whether metoprolol succinate or carvedilol could effectively reduce ventilatory overdrive with prolonged chronic therapy remains to be determined. It is important to consider that not all medications within a specific class were effective in treating the neurorespiratory system. Moreover, the pharmacological therapies that effectively treat the cardiovascular system may not offer effective treatment of the neurorespiratory system.

According to the American College of Cardiology/American Heart Association guidelines, ACE inhibitors or ARBs and β-ADR receptor blockers are the first-line pharmacotherapy for HF (*94*). Although the foundations of clinically classifying HF (New York Heart Association, CCS class) are largely based on dyspnea and exercise intolerance, clinical trials are generally not designed to include measures of respiratory function as a primary outcome. Dyspnea and reduced exercise capacity are the chief complaint of patients with HF for which respiratory muscle weakness is a contributing factor

(*14*, *95*). Thus, any improvements in respiratory function will benefit these patients.

Although diaphragm weakness is a salient feature of patients and experimental HF, until now, the incipient cause has remained elusive. Our findings establish the cause of diaphragm weakness and mechanisms by which it could be treated with appropriate therapy. However, whether treating the neurorespiratory system translates to improvements in quality of life and/or reduced mortality requires clinical evidence. Future clinical trials assessing efficacy of ARBs, β-ADR blockers, and new HF therapeutics would benefit from actively and quantitatively measuring respiratory function (that is, TTI) and symptomatology. Translating our study to improve clinical outcome in HF patients requires careful consideration of both drug class and type, in addition to titration for respiratory efficacy. In addition, evaluating the benefits of drug combinations should be considered in the design of future clinical trials.

MATERIALS AND METHODS

Study design

The objective of the present study was to identify the incipient cause and molecular mechanisms of diaphragm weakness in a pressure overload mouse model of HF. The sample sizes were determined on the basis of previous experience and taking into account the mortality rate of the surgical intervention. To ensure comparable degrees of cardiac dysfunction, echocardiography and/or invasive hemodynamic function was assessed in TAC mice at each experimental time point. Outliers were removed owing to absence of cardiac dysfunction and/or surgical intervention complications (infection, unsuccessful induction of pressure overload, excess surgical bleeding, etc.) in accordance with a ROUT outlier test at 2%. Mice were assigned to the respective study time points and/or experimental interventions at random, and with the exception of CSA analysis, experiments were conducted in a nonblinded fashion. Individual biological and technical replicates are indicated in the figure and table legends for each respective experiment and range between $4 < 14$ (biological) and $3 < 400$ (technical), depending on the specific technique.

All experimental procedures were approved by the Institutional Animal Care and Use Committee and conducted in accordance with the guidelines of the Canadian Council on Animal Care, as set out in the *Guide for the Care and Use of Experimental Animals*. All experiments were conducted on male CD-1 mice (Charles River Ltd.) housed in a 12:12 light-dark facility with food and water ad libitum at the University of Guelph.

Cardiac pressure overload induced by TAC or AAC

Nine-week-old mice (~35 g body weight) were anesthetized with an isoflurane/oxygen mix (2%:100%), intubated, and mechanically ventilated (Harvard Apparatus) at a tidal volume of 200 μl and at a rate of 150 breaths/min. The transverse aorta was constricted to the diameter of a 26-gauge needle to impose cardiac pressure overload, as previously described (*53*). Although TAC leads to hypertension proximal to the constriction, distally, slight hypotension can occur before restoration of systemic blood pressure. Thus, the abdominal aorta was constricted (AAC) in a subset of mice to investigate if the diaphragmatic myopathy observed in TAC could be attributed to hypotension-induced hypoperfusion. Animals were administered analgesic and carefully monitored for postsurgical complications. Those that displayed abnormalities or complications were removed from the study. Animals were used at 2, 4, 9, or 18 weeks after TAC or sham surgery.

Propranolol treatment

In a subset of TAC mice, propranolol was administered twice daily (8 a.m. and 6 p.m.) at a dose of 15 mg/kg, with the first injection immediately after TAC surgery. Mice were subsequently treated for either 2 or 4 weeks and were sacrificed after hemodynamic analysis for in vitro diaphragm contractility studies and histological, morphometric, and/or biochemical analysis.

Atenolol treatment

In a subset of mice, atenolol was administered twice daily (8 a.m. and 6 p.m.) at a dose of 15 mg/kg, with the first injection immediately after TAC surgery. Mice were subsequently treated for 4 weeks at which point P_{Iocc} was assessed before the mice were sacrificed for histological and molecular assessment.

Esophageal pressure measurements

Mice were anesthetized with an isoflurane/oxygen mix (2%:100%) and body temperature was maintained at 37°C. Mice were intubated using a 20-gauge angiocatheter (Becton, Dickinson and Company) to maintain an open and unobstructed airway. The angiocatheter was retrofitted with compressible tubing to facilitate inducible airway occlusions. Esophageal pressure (P_{es}) was measured with a 1.2F catheter (Transonic) recorded on LabScribe2 software (iWorx) and analyzed with Spike2 software (Cambridge Electronic Design). P_{es} was measured during five different protocols: (i) Eupneic breathing: Baseline P_{es} was measured at all time points of TAC, as previously discussed and analyzed for inspiratory pressure (P_I), inspiratory time (T_I), and respiratory frequency. (ii) Tracheal occlusions: Immediately after 2 min of baseline P_{es} recording, the trachea was occluded and P_{es} was monitored for changes. Tracheal occlusions were initiated at end expiratory volume to ensure consistency of the diaphragm length-tension relationship. Maximum inspiratory pressure (P_{Imax}) was evaluated after 25 s of occlusion when pressure generation reached a plateau. (iii) Pharmacological intervention in 2-week TAC mice: Baseline P_{es} was measured after injection of an ACE inhibitor (captopril; 15 mg/kg), ANGII receptor 1 antagonists (losartan and candesartan; 15 mg/kg), an ANG receptor 2 antagonist (PD123319; 10 mg/kg), and β-blockers (propranolol, atenolol, carvedilol, bisoprolol, and metoprolol; 15 mg/kg). All drugs (Sigma-Aldrich) were solubilized in sterile saline and administered via intraperitoneal injection. Measurements were obtained 1 hour after injection. (iv) Pharmacological intervention in sham mice: P_{es} was measured in sham mice during the infusion of isoproterenol, ANGII, or angiotensin1-7 fragment (ANG1-7). The right jugular vein was isolated, catheterized, and connected to a syringe pump (Harvard Apparatus) that infused 1×10^{-6} mol isoproterenol, ANGII, and ANG1-7 at varying rates. (v) Diaphragm EMG: Mice were ventilated at a rate of 150 breaths/min and a tidal volume of 200 μl before thoracotomy to expose the thoracic cavity and superior aspect of the diaphragm. EMG was obtained by placing two stainless steel recording electrodes on the superior aspect of the diaphragm, and bioelectrical signals were amplified and recorded (1 kHz) using LabScribe software. EMG signals were then integrated using Spike software to quantify the effect of ANGII infusion on EMG amplitude. Total volume did not exceed 5% of the estimated blood volume based on body weight. To account for any time-of-day variation in ventilatory drive, all P_{es} measurements were conducted between 9 a.m. and 11 a.m.

Hemodynamic analysis

Left and right ventricular function was assessed in mice anesthetized with an isoflurane/oxygen mix (2%:100%). Hemodynamic function was acquired using a 1.2F catheter (Transonic) advanced through the right common carotid artery or jugular vein and into the left or right ventricle, respectively. Pressure readings were digitized at 2 kHz and recorded using LabScribe2 analytic software (iWorx). After hemodynamic evaluation, mice were euthanized by exsanguination, and tissues were harvested for in vitro studies and histological and morphometric analysis or frozen at −80°C for biochemical and molecular analysis.

Lung compliance

Animals were anesthetized with sodium pentobarbital (30 to 45 mg/kg of body weight intraperitoneally) and placed in a supine position. The trachea was cannulated and connected by a three-way port to a ventilator (Harvard Apparatus), a Statham pressure transducer, and a graduated syringe. The pressure-volume relationship of the lung was determined by changing the lung volume at set increments with known functional residual capacity and by measuring the subsequent change in tracheal pressure (P_{tr}) 10 s after inflation. Before the subsequent measurement, lungs were inflated and ventilated for ~1 min to ensure constant volume history and to prevent atelectasis.

In vitro diaphragm contractility

Intact whole diaphragms were excised from the animal and placed in Krebs-Henseleit solution [NaCl (118 mM), KCl (4.7 mM), KH_2PO_4 (1.2 mM), $MgSO_4{\cdot}7H_2O$ (1.2 mM), $NaHCO_3$ (27.26 mM), glucose (11.1 mM), $CaCl_2{\cdot}2H_2O$ (2.3 mM), insulin (10 U/liter), and curare (3.0×10^{-4} g/liter)] at room temperature and pH 7.4. A section of muscle was removed from the costal portion of the right hemidiaphragm, with rib and central tendon intact. Silk ties were secured to both the central tendon and ribs and attached to a force transducer (Grass Instruments) and stationary hook, respectively. Stainless steel stimulating electrodes connected to a Grass electrical stimulator were placed on either side of the muscle section and used to elicit contractions via field stimulation. Tissue baths were placed such that each muscle was immersed in Krebs-Henseleit bicarbonate buffer continuously warmed to 27°C and aerated with 95% O_2:5% CO_2. After setting the optimal muscle length and after a 45-min thermoequilibration period, peak force and rate of force production ($+dT/dt_{max}$) were determined during a force-frequency test (one contraction every 30 s with a train duration of 250 ms). In addition, diaphragm fatigability and passive force production were determined during repeated submaximal stimulations (40 Hz; 150 contractions per minute for 3 min). Isometric contractility data were collected using AcqKnowledge software (BIOPAC Systems) and analyzed using Spike2 software. Force production and contractility were normalized to muscle weight (in milligrams) to account for differences in diaphragm tissue size.

Isolated myofilament preparation

After excision of the diaphragm, myofilaments were isolated and permeabilized, as previously described (*48*, *92*, *93*). Briefly, diaphragm muscle was relaxed and then skinned with 1% Triton X-100 overnight at 4°C. After skinning, isolated myofilaments were dissected from the diaphragm and attached to aluminum "T-clips." The T-clips and myofilaments were then attached to the force transducer and servomotor and stretched to a sarcomere length of 2.3 μm while being maintained at pH 7.0 and 15° ± 1°C. To determine contractile function, isolated myofilaments were exposed to various concentrations of Ca^{2+} between pCa 9.0 and pCa 5.0 while simultaneously measuring force production, cross-bridge kinetics, and calcium sensitivity.

Histology

For histological analysis of skeletal muscle, mice were perfused with 50 mM KCl in phosphate-buffered saline (10 ml) and then 10% neutral buffered formalin (NBF) (10 ml). Lungs were excised, and perfusion was fixed with NBF at a constant pressure of 20 cmH_2O overnight. All tissues were then fixed for an additional 48 hours in NBF and stored in 70% ethanol. Processed tissues were embedded in paraffin wax (Thermo Fisher Scientific), and 5-μm tissue sections were mounted on charged 1.2-mm superfrost slides (Thermo Fisher Scientific). Diaphragm and limb muscle sections were stained using modified Harris hematoxylin (Thermo Fisher Scientific) and eosin (Thermo Fisher Scientific) or picrosirius red (Aqueous Picric acid and Direct Red 80, both from Sigma-Aldrich); lung sections were also stained with Gomori's one-step trichrome (Thermo Fisher Scientific). All sections were imaged using an Olympus FSX100 light microscope (Olympus) and analyzed in Cell Sense software for fibrosis analysis (Olympus) or Image J for CSA analysis; all quantifications were carried out in a blinded manner.

Gene expression analysis using real-time PCR

Fifty milligrams of diaphragm tissue was placed in a 2-ml tube containing 1.4-mm ceramic spheres and 1 ml of TRIzol (Invitrogen) and homogenized using the FastPrep-24 system. Samples were processed at maximum speed for 60 s twice. After centrifugation, samples were transferred into new 1.5-ml tubes with 200 μl of chloroform and centrifuged at high speed for 15 min. The clear supernatant, containing the RNA fraction, was subsequently transferred to a new 1.5-ml tube with 500 μl of isopropanol. Samples were then purified with the Qiagen RNeasy kit. DNase treatment was performed on-column with the RNase-Free DNase set (Qiagen). The concentration of mRNA was quantified using a spectrophotometer (NanoDrop, ND1000, Thermo Fisher Scientific). RNA was reverse-transcribed into complementary DNA (cDNA) using qScript cDNA Supermix (Quanta Biosciences). All reactions were performed in T100 thermal cycler (Bio-Rad). cDNA was stored overnight at 4°C or used immediately for real-time PCR.

Primers were designed using IDT Integrated DNA Technologies software. Each analysis was performed in a total volume of 20 μl of reaction mixture containing 2 μl of cDNA sample (diluted 1:2), 10 μl of SsoFast EvaGreen Supermix (Bio-Rad), 7 μl of RNase-free water, and 1 μl of gene-specific sense and antisense primers. qPCR was performed using the CFX Connect Real-Time PCR system with CFX Manager software (Bio-Rad). PCR cycle conditions were 95°C for 3 min (one cycle), 95°C for 10 s, and 60°C for 30 s (40 cycles).

Preliminary studies showed that *Hmbs* was a stable gene over 18 weeks of TAC and thus was chosen as a reference gene for all molecular data. Fold changes between sham and treated samples were then calculated as $2^{(\Delta C_t\ \mathrm{TAC} - \Delta C_t\ \mathrm{sham})}$, with ΔC_t indicating normalized values.

Western blotting

Powdered tissue samples were homogenized on ice in fresh NP-40–based lysis buffer with activated sodium orthovanadate, a phosphatase inhibitor cocktail (524628, Calbiochem), and a protease inhibitor cocktail (P8340, Sigma-Aldrich). Samples were placed on ice for 30 min before centrifugation at 2000 relative centrifugal force (rcf)

for 2 min at 4°C. The supernatant was transferred to a fresh microcentrifuge tube and centrifuged at 1200 rcf for 30 min at 4°C. The supernatant was then transferred to a fresh microcentrifuge tube using a 28 $^{1}/_{2}$-gauge insulin syringe to shear DNA in the remaining sample. Total protein content was measured by bicinchoninic acid assay to ensure equal protein loading (13 μg per lane). Samples were separated via SDS–polyacrylamide gel electrophoresis (5671095, Bio-Rad) and transferred to nitrocellulose membrane (1620112, Bio-Rad) for immunoblotting. To ensure equal total protein loading and uniform protein transfer, membranes were reversibly stained with MemCode (24580, Thermo Fisher Scientific) before probing. Membranes were then blocked in 5% milk and incubated in a primary anti-phospho EIF2α (Ser^{51}) antibody (1:1000; 9721S, Cell Signaling; 1% milk in 1× TBST with 4% sodium azide) overnight at 4°C. Membranes were washed in 1× TBST and subsequently incubated with a goat anti-rabbit horseradish peroxidase–conjugated secondary antibody (1:1000; 2054, Santa Cruz Biotechnology; 5% milk for 2 hours). Signal was detected through enhanced chemiluminescence (34076, Thermo Fisher Scientific) and digital imaging (1708280, Bio-Rad). Densitometric quantification was completed using Image Lab software (Bio-Rad). Values were obtained by measuring the target band relative to the total protein of the lane.

Statistics

Values presented are mean ± SEM unless otherwise indicated. Graphical and statistical analyses were completed using GraphPad (Prism 6, GraphPad Software Inc.). Unpaired Student's *t* tests were used for comparison between two groups. For the comparison between three or more groups, a protected LSD test was used to determine significance. Significance was determined at $P < 0.05$.

SUPPLEMENTARY MATERIALS

www.sciencetranslationalmedicine.org/cgi/content/full/9/390/eaag1303/DC1

Fig. S1. TAC induces progressive interstitial fibrosis in the diaphragm.

Fig. S2. TAC induces biphasic and transient increases in diaphragm in vitro–specific force production, contractility, and passive baseline force.

Fig. S3. AAC induces diaphragmatic atrophy and fibrosis.

Fig. S4. Peripheral limb muscle CSA is unaffected in mice at 4 weeks of TAC.

Fig. S5. Propranolol and atenolol treatment in sham mice induces alterations in diaphragm gene expression profile.

Fig. S6. Propranolol and atenolol treatment in TAC mice induces alterations in diaphragm gene expression profile.

Table S1. TAC induces progressive changes in hemodynamics, morphometrics, and metabolic parameters throughout 18 weeks of pressure overload.

Table S2. Pressure overload imposed by 18 weeks of AAC induces hemodynamic and morphometric alterations similar to 9 weeks of TAC.

Table S3. Indices of systolic and diastolic dysfunction persist in 2-week and 4-week TAC mice treated with propranolol.

REFERENCES AND NOTES

1. P. A. McCullough, E. F. Philbin, J. A. Spertus, S. Kaatz, K. R. Sandberg, W. D. Weaver, Confirmation of a heart failure epidemic: Findings from the Resource Utilization Among Congestive Heart Failure (REACH) study. *J. Am. Coll. Cardiol.* **39**, 60–69 (2002).
2. J. B. Croft, W. H. Giles, R. A. Pollard, N. L. Keenan, M. L. Casper, R. F. Anda, Heart failure survival among older adults in the United States: A poor prognosis for an emerging epidemic in the Medicare population. *Arch. Intern. Med.* **159**, 505–510 (1999).
3. A. L. Bui, T. B. Horwich, G. C. Fonarow, Epidemiology and risk profile of heart failure. *Nat. Rev. Cardiol.* **8**, 30–41 (2011).
4. L. Liu, H. J. Eisen, Epidemiology of heart failure and scope of the problem. *Cardiol. Clin.* **32**, 1–8 (2014).
5. A. Apostolo, G. Giusti, P. Gargiulo, M. Bussotti, P. Agostoni, Lungs in heart failure. *Pulm. Med.* **2012**, 952741 (2012).
6. S. Azarbar, J. Dupuis, Lung capillary injury and repair in left heart disease: A new target for therapy? *Clin. Sci.* **127**, 65–76 (2014).
7. Y. Chen, H. Guo, D. Xu, X. Xu, H. Wang, X. Hu, Z. Lu, D. Kwak, Y. Xu, R. Gunther, Y. Huo, E. K. Weir, Left ventricular failure produces profound lung remodeling and pulmonary hypertension in mice: Heart failure causes severe lung disease. *Hypertension* **59**, 1170–1178 (2012).
8. S. A. Evans, L. Watson, A. J. Cowley, I. D. Johnston, W. J. Kinnear, Static lung compliance in chronic heart failure: Relation with dyspnoea and exercise capacity. *Thorax* **50**, 245–248 (1995).
9. B. K. Gehlbach, E. Geppert, The pulmonary manifestations of left heart failure. *Chest* **125**, 669–682 (2004).
10. K. Kee, M. T. Naughton, Heart failure and the lung. *Circ. J.* **74**, 2507–2516 (2010).
11. N. Ambrosino, C. Opasich, P. Crotti, F. Cobelli, L. Tavazzi, C. Rampulla, Breathing pattern, ventilatory drive and respiratory muscle strength in patients with chronic heart failure. *Eur. Respir. J.* **7**, 17–22 (1994).
12. A. Filusch, R. Ewert, M. Altesellmeier, C. Zugck, R. Hetzerm M. M. Borst, H. A. Katus, F. J. Meyer, Respiratory muscle dysfunction in congestive heart failure—The role of pulmonary hypertension. *Int. J. Cardiol.* **150**, 182–185 (2011).
13. M. D. Hammond, K. A. Bauer, J. T. Sharp, R. D. Rocha, Respiratory muscle strength in congestive heart failure. *Chest* **98**, 1091–1094 (1990).
14. D. M. Mancini, D. Henson, J. LaManca, S. Levine, Respiratory muscle function and dyspnea in patients with chronic congestive heart failure. *Circulation* **86**, 909–918 (1992).
15. C. McParland, B. Krishnan, Y. Wang, C. G. Gallagher, Inspiratory muscle weakness and dyspnea in chronic heart failure. *Am. Rev. Respir. Dis.* **146**, 467–472 (1992).
16. A. De Troyer, M. Estenne, J. C. Yernault, Disturbance of respiratory muscle function in patients with mitral valve disease. *Am. J. Med.* **69**, 867–873 (1980).
17. G. Supinski, A. DiMarco, M. Dibner-Dunlap, Alterations in diaphragm strength and fatiguability in congestive heart failure. *J. Appl. Physiol.* **76**, 2707–2713 (1994).
18. Y. Lecarpentier, C. Coirault, O. Langeron, F. X. Blanc, S. Salmeron, P. Attal, B. Riou, D. Chemla, Impaired load dependence of diaphragm relaxation during congestive heart failure in the rabbit. *J. Appl. Physiol.* **87**, 1339–1345 (1999).
19. C. Coirault, O. Langeron, F. Lambert, F.-X. Blanc, G. Lerebours, N. Claude, B. Riou, D. Chelma, Y. Lecarpentier, Impaired skeletal muscle performance in the early stage of cardiac pressure overload in rabbits: Beneficial effects of angiotensin-converting enzyme inhibition. *J. Pharmacol. Exp. Ther.* **291**, 70–75 (1999).
20. B. A. Tikunov, D. Mancini, S. Levine, Changes in myofibrillar protein composition of human diaphragm elicited by congestive heart failure. *J. Mol. Cell. Cardiol.* **28**, 2537–2541 (1996).
21. G. Stassijns, R. Lysens, M. Decramer, Peripheral and respiratory muscles in chronic heart failure. *Eur. Respir. J.* **9**, 2161–2167 (1996).
22. G. Stassijns, G. Gayan-Ramirez, P. De Leyn, G. Verhoeven, P. Herijgers, V. de Bock, R. Dom, R. Lysens, M. Decramer, Systolic ventricular dysfunction causes selective diaphragm atrophy in rats. *Am. J. Respir. Crit. Care Med.* **158**, 1963–1967 (1998).
23. N. G. MacFarlane, G. M. Darnley, G. L. Smith, Cellular basis for contractile dysfunction in the diaphragm from a rabbit infarct model of heart failure. *Am. J. Physiol. Cell Physiol.* **278**, C739–C746 (2000).
24. P. K. Lunde, A. J. Dahlstedt, J. D. Bruton, J. Lännergren, P. Thorén, O. M. Sejersted, H. Westerblad, Contraction and intracellular Ca^{2+} handling in isolated skeletal muscle of rats with congestive heart failure. *Circ. Res.* **88**, 1299–1305 (2001).
25. C. Coirault, A. Guellich, T. Barby, J. L. Samuel, B. Riou, Y. Lecarpentier, Oxidative stress of myosin contributes to skeletal muscle dysfunction in rats with chronic heart failure. *Am. J. Physiol. Heart Circ. Physiol.* **292**, H1009–H1017 (2007).
26. M. Hayot, P. F. Perrigault, V. Gautier-Dechaud, X. Capdevilla, J. Millic-Emill, C. Prefaut, M. Ramonatxo, Tension-time index of inspiratory muscles in COPD patients: Role of airway obstruction. *Respir. Med.* **92**, 828–835 (1998).
27. D. Devroey, V. Van Casteren, Signs for early diagnosis of heart failure in primary health care. *Vasc. Health Risk Manag.* **7**, 591–596 (2011).
28. H. Mahdyoon, R. Klein, W. Eyler, J. B. Lakier, S. C. Chakko, M. Gheorghiade, Radiographic pulmonary congestion in end-stage congestive heart failure. *Am. J. Cardiol.* **63**, 625–627 (1989).
29. M. Gheorghiade, F. Follath, P. Ponikowski, J. H. Barsuk, J. E. Blair, J. G. Cleland, K. Dickstein, M. H. Drazner, G. C. Fonarow, T. Jaarsma, G. Jondeau, J. L. Sendon, A. Mebazaa, M. Metra, M. Niemenin, P. S. Pang, P. Seferovic, L. W. Stevenson, D. J. van Veldhuisen, F. Zannad, S. D. Anker, A. Rhodes, J. J. V. McMurray, G. Filippatos, Assessing and grading congestion in acute heart failure: A scientific statement from the acute heart failure committee of the heart failure association of the European Society of Cardiology and endorsed by the European Society of Intensive Care Medicine. *Eur. J. Heart Fail.* **12**, 423–433 (2010).
30. M. C. Michel, C. Foster, H. R. Brunner, L. Liu, A systematic comparison of the properties of clinically used angiotensin II type 1 receptor antagonists. *Pharmacol. Rev.* **65**, 809–848 (2013).
31. S. E. Kjeldsen, J. Stelhammar, P. Hasvold, J. Bodehgard, U. Olsson, D. Russell, Effects of losartan vs candesartan in reducing cardiovascular events in the primary treatment of hypertension. *J. Hum. Hypertens.* **24**, 263–273 (2010).

32. D. M. Mancini, J. La Manca, L. Donchez, D. Henson, S. Levine, The sensation of dyspnea during exercise is not determined by the work of breathing in patients with heart failure. *J. Am. Coll. Cardiol.* **28**, 391–395 (1996).
33. H. A. Rockman, R. S. Ross, A. N. Harris, K. U. Knowlton, M. E. Steinhelper, L. J. Field, J. Ross Jr., K. R. Chien, Segregation of atrial-specific and inducible expression of an atrial natriuretic factor transgene in an in vivo murine model of cardiac hypertrophy. *Proc. Natl. Acad. Sci. U.S.A.* **88**, 8277–8281 (1991).
34. P. Davey, T. Meyer, A. Coats, S. Adamopoulos, B. Cessadei, J. Conway, P. Sleight, Ventilation in chronic heart failure: Effects of physical training. *Br. Heart J.* **68**, 473–477 (1992).
35. L. A. Wolfe, J. G. Kemp, A. P. Heenan, R. J. Preston, P. J. Ohtake, Acid-base regulation and control of ventilation in human pregnancy. *Can. J. Physiol. Pharmacol.* **76**, 815–827 (1998).
36. L. Nettlefold, D. Jensen, I. Janssen, L. A. Wolfe, Ventilatory control and acid–base regulation across the menstrual cycle in oral contraceptive users. *Respir. Physiol. Neurobiol.* **158**, 51–58 (2007).
37. L. Barki-Harrington, L. M. Luttrell, H. A. Rockman, Dual inhibition of β-adrenergic and angiotensin II receptors by a single antagonist: A functional role for receptor–receptor interaction in vivo. *Circulation* **108**, 1611–1618 (2003).
38. P. Gohlke, T. Kox, T. Jürgensen, S. von Kügelgen, W. Rascher, T. Unger, J. Culman, Peripherally applied candesartan inhibits central responses to angiotensin II in conscious rats. *Naunyn Schmiedebergs Arch. Pharmacol.* **365**, 477–483 (2002).
39. P. Gohlke, S. von Kügelgen, T. Jürgensen, T. Kox, W. Rascher, J. Culman, T. Unger, Effects of orally applied candesartan cilexetil on central responses to angiotensin II in conscious rats. *J. Hypertens.* **20**, 909–918 (2002).
40. Y. Nishimura, T. Ito, K.-L. Hoe, J. M. Saavedra, Chronic peripheral administration of the angiotensin II AT_1 receptor antagonist candesartan blocks brain AT_1 receptors. *Brain Res.* **871**, 29–38 (2000).
41. J. Zhuo, I. Moeller, T. Jenkins, S. Y. Chai, A. M. Allen, M. Ohishi, F. A. O. Mendelsohn, Mapping tissue angiotensin-converting enzyme and angiotensin AT1, AT2 and AT4 receptors. *J. Hypertens.* **16**, 2027–2037 (1998).
42. J. Zhuo, C. Maric, P. J. Harris, D. Alcorn, F. A. O. Mendelsohn, Localization and functional properties of angiotensin II AT_1 receptors in the kidney: Focus on renomedullary interstitial cells. *Hypertens. Res.* **20**, 233–250 (1997).
43. M. Macova, J. Pavel, J. M. Saavedra, A peripherally administered, centrally acting angiotensin II AT_2 antagonist selectively increases brain AT_1 receptors and decreases brain tyrosine hydroxylase transcription, pituitary vasopressin and ACTH. *Brain Res.* **1250**, 130–140 (2009).
44. J. D. Bui, B. Kimura, M. I. Phillips, Losartan potassium, a nonpeptide antagonist of angiotensin II, chronically administered p.o. does not readily cross the blood-brain barrier. *Eur. J. Pharmacol.* **219**, 147–151 (1992).
45. G. Neil-Dwyer, J. Bartlett, J. McAinsh, J. M. Cruickshank, Beta-adrenoceptor blockers and the blood-brian barrier. *Br. J. Clin. Pharmacol.* **11**, 549–553 (1981).
46. J. J. Hakkarainen, A. J. Jalkanen, T. M. Kääriäinen, P. Keski-Rahkonen, T. Venäläinen, J. Hokkanen, J. Mönkkönen, M. Suhonen, M. M. Forsberg, Comparison of in vitro cell models in predicting in vivo brain entry of drugs. *Int. J. Pharm.* **402**, 27–36 (2010).
47. P. P. de Tombe, Cardiac myofilaments: Mechanics and regulation. *J. Biomech.* **36**, 721–730 (2003).
48. R. J. Solaro, T. Kobayashi, Protein phosphorylation and signal transduction in cardiac thin filaments. *J. Biol. Chem.* **286**, 9935–9940 (2011).
49. R. J. Solaro, M. Henze, T. Kobayashi, Integration of troponin I phosphorylation with cardiac regulatory networks. *Circ. Res.* **112**, 355–366 (2013).
50. A. Kushnir, A. R. Marks, The ryanodine receptor in cardiac physiology and disease. *Adv. Pharmacol.* **59**, 1–30 (2010).
51. X. H. Wehrens, A. R. Marks, Molecular determinants of altered contractility in heart failure. *Ann. Med.* **36** (suppl. 1), 70–80 (2004).
52. T. E. Gillis, J. M. Klaiman, A. J. Foster, M. J. Platt, J. S. Huber, M. Y. Corso, J. A. Simpson, Dissecting the role of the myofilament in diaphragm dysfunction during the development of heart failure in mice. *Am. J. Physiol. Heart Circ. Physiol.* **310**, H572–H586 (2016).
53. M. Periasamy, A. Kalyanasundaram, SERCA pump isoforms: Their role in calcium transport and disease. *Muscle Nerve* **35**, 430–442 (2007).
54. D. Ron, Translational control in the endoplasmic reticulum stress response. *J. Clin. Invest.* **110**, 1383–1388 (2002).
55. K. Zhang, R. J. Kaufman, From endoplasmic-reticulum stress to the inflammatory response. *Nature* **454**, 455–462 (2008).
56. H. P. Kim, H.-O. Pae, S. H. Back, S. W. Chung, J. M. Woo, Y. Son, H.-T. Chung, Heme oxygenase-1 comes back to endoplasmic reticulum. *Biochem. Biophys. Res. Commun.* **404**, 1–5 (2011).
57. M. A. Allwood, R. T. Kinobe, L. Ballantyne, N. Romanova, L. G. Melo, C. A. Ward, K. R. Brunt, J. A. Simpson, Heme oxygenase-1 overexpression exacerbates heart failure with aging and pressure overload but is protective against isoproterenol-induced cardiomyopathy in mice. *Cardiovasc. Pathol.* **23**, 231–237 (2014).
58. H. W. H. van Hees, H. F. M. van der Heijden, T. Hafmans, L. Ennen, L. M. A. Heunks, F. W. A. Verheugt, P. N. R. Dekhuijzen, Impaired isotonic contractility and structural abnormalities in the diaphragm of congestive heart failure rats. *Int. J. Cardiol.* **128**, 326–335 (2008).
59. Y. T. Yang, M. A. McElligott, Multiple actions of β-adrenergic agonists on skeletal muscle and adipose tissue. *Biochem. J.* **261**, 1–10 (1989).
60. G. A. Ordway, P. D. Neufer, E. R. Chin, G. N. DeMartino, Chronic contractile activity upregulates the proteasome system in rabbit skeletal muscle. *J. Appl. Physiol.* **88**, 1134–1141 (2000).
61. S. R. Kimball, P. A. Farrell, L. S. Jefferson, Invited Review: Role of insulin in translational control of protein synthesis in skeletal muscle by amino acids or exercise. *J. Appl. Physiol.* **93**, 1168–1180 (2002).
62. G. L. Dohm, E. B. Tapscott, H. A. Barakat, G. J. Kasperek, Measurement of in vivo protein synthesis in rats during an exercise bout. *Biochem. Med.* **27**, 367–373 (1982).
63. J. Wu, J. L. Ruas, J. L. Estall, K. A. Rasbach, J. H. Choi, L. Ye, P. Boström, H. M. Tyra, R. W. Crawford, K. P. Campbell, D. T. Rutkowski, R. J. Kaufman, B. M. Spiegelman, The unfolded protein response mediates adaptation to exercise in skeletal muscle through a PGC-1α/ATF6α complex. *Cell Metab.* **13**, 160–169 (2011).
64. M. Boyce, K. F. Bryant, C. Jousse, K. Long, H. P. Harding, D. Scheuner, R. J. Kaufman, D. Ma, D. M. Coen, D. Ron, J. Yuan, A selective inhibitor of eIF2α dephosphorylation protects cells from ER stress. *Science* **307**, 935–939 (2005).
65. P. D. Lu, C. Jousse, S. J. Marciniak, Y. Zhang, I. Novoa, D. Scheuner, R. J. Kaufman, D. Ron, H. P. Harding, Cytoprotection by pre-emptive conditional phosphorylation of translation initiation factor 2. *EMBO J.* **23**, 169–179 (2004).
66. H. P. Harding, Y. Zhang, A. Bertolotti, H. Zeng, D. Ron, *Perk* is essential for translational regulation and cell survival during the unfolded protein response. *Mol. Cell* **5**, 897–904 (2000).
67. H. Zinszner, M. Kuroda, X. Wang, N. Batchvarova, R. T. Lightfoot, H. Remotti, J. L. Stevens, D. Ron, CHOP is implicated in programmed cell death in response to impaired function of the endoplasmic reticulum. *Genes Dev.* **12**, 982–995 (1998).
68. J. H. Lin, H. Li, D. Yasumura, H. R. Cohen, C. Zhang, B. Panning, K. M. Shokat, M. M. Lavail, P. Walter, IRE1 signaling affects cell fate during the unfolded protein response. *Science* **318**, 944–949 (2007).
69. J. H. Lin, H. Li, Y. Zhang, D. Ron, P. Walter, Divergent effects of PERK and IRE1 signaling on cell viability. *PLOS ONE* **4**, e4170 (2009).
70. J. M. Saavedra, Brain angiotensin II: New developments, unanswered questions and therapeutic opportunities. *Cell. Mol. Neurobiol.* **25**, 485–512 (2005).
71. J. M. Saavedra, Emerging features of brain angiotensin receptors. *Regul. Pept.* **85**, 31–45 (1999).
72. M.-O. Guimond, N. Gallo-Payet, The angiotensin II type 2 receptor in brain functions: An update. *Int. J. Hypertens.* **2012**, 351758 (2012).
73. A. M. Allen, I. Moeller, T. A. Jenkins, J. Zhuo, G. P. Aldred, S. Y. Chai, F. A. O. Mendelsohn, Angiotensin receptors in the nervous system. *Brain Res. Bull.* **47**, 17–28 (1998).
74. E. C. Li, B. S. Heran, J. M. Wright, Angiotensin converting enzyme (ACE) inhibitors versus angiotensin receptor blockers for primary hypertension. *Cochrane Database Syst. Rev.* **8**, CD009096 (2014).
75. J. A. Simpson, K. R. Brunt, C. P. Collier, S. Iscoe, Hyperinflation-induced cardiorespiratory failure in rats. *J. Appl. Physiol.* **107**, 275–282 (2009).
76. J. A. Simpson, K. R. Brunt, S. Iscoe, Repeated inspiratory occlusions acutely impair myocardial function in rats. *J. Physiol.* **586**, 2345–2355 (2008).
77. J. A. Simpson, S. Iscoe, Cardiorespiratory failure in rat induced by severe inspiratory resistive loading. *J. Appl. Physiol.* **102**, 1556–1564 (2007).
78. J. A. Simpson, S. Iscoe, Hypoxia, not hypercapnia, induces cardiorespiratory failure in rats. *Respir. Physiol. Neurobiol.* **196**, 56–62 (2014).
79. M. J. Kendall, Clinical relevance of pharmacokinetic differences between beta blockers. *Am. J. Cardiol.* **80**, 15J–19J (1997).
80. R. Bølling, N. M. Scheller, L. Køber, H. E. Poulsen, G. H. Gislason, C. Torp-Pedersen, Comparison of the clinical outcome of different beta-blockers in heart failure patients: A retrospective nationwide cohort study. *Eur. J. Heart Fail.* **16**, 678–684 (2014).
81. M. J. Domanski, H. Krause-Steinrauf, B. M. Massie, P. Deedwania, D. Follmann, D. Kovar, D. Murray, R. Oren, Y. Rosenberg, J. Young, M. Zille, E. Eichhorn; BEST Investigators, A comparative analysis of the results from 4 trials of β-blocker therapy for heart failure: BEST, CIBIS-II, MERIT-HF, and COPERNICUS. *J. Card. Fail.* **9**, 354–363 (2003).
82. Y.-M. He, X.-J. Yang, X. Zhao, X.-J. Cheng, H.-F. Xu, Y. X. Qian, X. Li, β-Blockers in heart failure: Benefits of β-blockers according to varying male proportions of study patients. *Clin. Cardiol.* **35**, 505–511 (2012).
83. Å. Hjalmarson, Cardioprotection with beta-adrenoceptor blockers. Does lipophilicity matter? *Basic Res. Cardiol.* **95** (suppl. 1), I41–I45 (2000).
84. M. C. S. Wong, W. W. S. Tam, X. Q. Lao, H. H. Wang, M. W. Kwan, C. S. Cheung, E. L. H. Tong, N. T. Cheung, B. P. Yan, C. M. Yu, S. M. Griffiths, The effectiveness of metoprolol versus atenolol on prevention of all-cause and cardiovascular mortality in a large Chinese population: A cohort study. *Int. J. Cardiol.* **175**, 425–432 (2014).

85. J. J. DiNicolantonio, C. J. Lavie, H. Fares, A. R. Menezes, J. H. O'Keefe, Meta-analysis of *carvedilol* versus beta 1 selective beta-blockers (*atenolol*, *bisoprolol*, *metoprolol*, and *nebivolol*). *Am. J. Cardiol.* **111**, 765–769 (2013).
86. W. J. Remme, J. G. Cleland, L. Erhardt, P. Spark, C. Torp-Pedersen, M. Metra, M. Komajda, C. Moullet, M. A. Lukas, P. Poole-Wilson, A. Di Lenarda, K. Swedberg, Effect of carvedilol and metoprolol on the mode of death in patients with heart failure. *Eur. J. Heart Fail.* **9**, 1128–1135 (2007).
87. B. Pasternak, H. Svanström, M. Melbye, A. Hviid, Association of treatment with carvedilol vs metoprolol succinate and mortality in patients with heart failure. *JAMA Intern. Med.* **174**, 1597–1604 (2014).
88. J. Wikstrand, H. Wedel, D. Castagno, J. J. V. McMurray, The large-scale placebo-controlled beta-blocker studies in systolic heart failure revisited: Results from CIBIS-II, COPERNICUS and SENIORS-SHF compared with stratified subsets from MERIT-HF. *J. Intern. Med.* **275**, 134–143 (2014).
89. A. Briasoulis, M. Palla, L. Afonso, Meta-analysis of the effects of carvedilol versus metoprolol on all-cause mortality and hospitalizations in patients with heart failure. *Am. J. Cardiol.* **115**, 1111–1115 (2015).
90. A. S. Go, J. Yang, J. H. Gurwitz, J. Hsu, K. Lane, R. Platt, Comparative effectiveness of beta-adrenergic antagonists (*atenolol*, *metoprolol tartrate*, *carvedilol*) on the risk of rehospitalization in adults with heart failure. *Am. J. Cardiol.* **100**, 690–696 (2007).
91. A. S. Go, J. Yang, J. H. Gurwitz, J. Hsu, K. Lane, R. Platt, Comparative effectiveness of different β-adrenergic antagonists on mortality among adults with heart failure in clinical practice. *Arch. Intern. Med.* **168**, 2415–2421 (2008).
92. K. U. Buhring, H. Sailer, H. P. Faro, G. Leopold, J. Pabst, A. Garbe, Pharmacokinetics and metabolism of bisoprolol-14C in three animal species and in humans. *J. Cardiovasc. Pharmacol.* **8** (suppl. 11), S21–S28 (1986).
93. K. Leung, in *Molecular Imaging and Contrast Agent Database (MICAD)* (National Center for Biotechnology Information, 2004).
94. C. W. Yancy, M. Jessup, B. Bozkurt, J. Butler, D. E. Casey Jr., M. H. Drazner, G. C. Fonarow, S. A. Geraci, T. Horwich, J. L. Januzzi, M. R. Johnson, E. K. Kasper, W. C. Levy, F. A. Masoudi, P. E. McBride, J. J. Murray, J. E. Mitchell, P. N. Peterson, B. Riegel, F. Sam, L. W. Stevenson, W. H. W. Tang, E. J. Tasi, B. L. Wilkoff, 2013 ACCF/AHA guideline for the management of heart failure: A report of the American College of Cardiology Foundation/American Heart Association Task Force on Practice Guidelines. *J. Am. Coll. Cardiol.* **62**, e147–e239 (2013).
95. D. M. Mancini, Pulmonary factors limiting exercise capacity in patients with heart failure. *Prog. Cardiovasc. Dis.* **37**, 347–370 (1995).

Acknowledgments: We express our thanks to B. Neel and S. Iscoe for their helpful discussion and comments, J. Fisher for technical guidance on pulmonary mechanics, and I. Smith for the computer graphic illustration. **Funding:** This work was funded by grants from the Ontario Thoracic Society (to J.A.S.), the Canadian Institutes of Health Research (MOP111159 to J.A.S.), and the Natural Sciences and Engineering Research Council (to J.A.S., K.R.B., and T.E.G.). J.A.S. is a new investigator with the Heart and Stroke Foundation of Ontario. A.J.F. was supported by the Canadian Lung Association/Canadian Thoracic Society Studentship. A.J.F. and M.J.P. were both supported by the Ontario Graduate Scholarship. A.M.A. was supported by a grant from the University of Guelph-Humber Research Fund. We further acknowledge J. Southen and B. Southen of London, Ontario, for their philanthropic support. **Author contributions:** A.J.F., K.R.B., and J.A.S. conceptualized the study and designed the experiments. A.J.F., M.J.P., J.S.H., A.L.E., A.M.A., N.R., T.E.G., K.R.B., and J.A.S. conducted the experiments. All authors analyzed and/or interpreted the experimental results. A.J.F., K.R.B., and J.A.S. drafted the manuscript, critically revised the manuscript for intellectual content, and gave the final approval of the article. All authors have read and given permission to the final draft of the manuscript. **Competing interests:** The authors declare that they have no competing interests.

Submitted 12 May 2016
Accepted 13 March 2017
Published 17 May 2017
10.1126/scitranslmed.aag1303

Citation: A. J. Foster, M. J. Platt, J. S. Huber, A. L. Eadie, A. M. Arkell, N. Romanova, D. C. Wright, T. E. Gillis, C. L. Murrant, K. R. Brunt, J. A. Simpson, Central-acting therapeutics alleviate respiratory weakness caused by heart failure–induced ventilatory overdrive. *Sci. Transl. Med.* **9**, eaag1303 (2017).